TGF-β blockade drives a transitional effector phenotype in T cells reversing SIV latency and decreasing SIV reservoirs *in vivo*

Jinhee Kim[1], Deepanwita Bose[2]†, Mariluz Araínga[2]†, Muhammad R. Haque[3], Christine M Fennessey[4], Rachel A Caddell[5], Yanique Thomas[3], Douglas E Ferrell[2], Syed Ali[2], Emanuelle Grody[3,6], Yogesh Goyal[3,6,7], Claudia Cicala[8], James Arthos[8], Brandon F Keele[4], Monica Vaccari[5,9], Ramon Lorenzo-Redondo[1,10], Thomas J Hope[3], Francois Villinger[2] and Elena Martinelli[1]

[1]Department of Medicine, Division of Infectious Diseases, Feinberg School of Medicine, Northwestern University, Chicago, IL, USA
[2]New Iberia Research Center, University of Louisiana at Lafayette, New Iberia, LA, USA
[3]Cell and Developmental Biology, Feinberg School of Medicine, Northwestern University, Chicago, IL, USA
[4]AIDS and Cancer Virus Program, Frederick National Laboratory for Cancer Research, Frederick MD
[5]Division of Immunology, Tulane National Primate Research Center, Covington LA, USA
[6]Center for Synthetic Biology, Northwestern University, Chicago, IL, USA
[7]Robert H. Lurie Comprehensive Cancer Center, Feinberg School of Medicine, Northwestern University, Chicago, IL, USA
[8]Laboratory of Immunoregulation, National Institute of Allergy and Infectious Diseases, National Institutes of Health, Bethesda, MD, USA
[9]Department of Microbiology and Immunology, Tulane University School of Medicine, New Orleans, LA, USA
[10]Center for Pathogen Genomics and Microbial Evolution, Northwestern University Havey Institute for Global Health, Chicago, IL, USA.

† Equal contributors
*Corresponding author:

Elena Martinelli

elena.martinelli@northwestern.edu

One-sentence summary:

TGF-β blockade drives an effector phenotype in immune cells leading to SIV latency reversal and enhanced immune responses in vivo.

Abstract

HIV-1 persistence during ART is due to the establishment of long-lived viral reservoirs in resting immune cells. Using an NHP model of barcoded SIVmac239 intravenous infection and therapeutic dosing of anti-TGFBR1 inhibitor galunisertib (LY2157299), we confirm the latency reversal properties of *in vivo* TGF-β blockade, decrease viral reservoirs and stimulate immune responses. Treatment of eight female, SIV-infected macaques on ART with four 2-weeks cycles of galunisertib leads to viral reactivation as indicated by plasma viral load and immunoPET/CT with a ^{64}Cu-DOTA-F(ab')$_2$-p7D3-probe. Post-galunisertib, lymph nodes, gut and PBMC exhibit lower cell-associated (CA-)SIV DNA and lower intact pro-virus (PBMC). Galunisertib does not lead to systemic increase in inflammatory cytokines. High-dimensional cytometry, bulk, and single-cell (sc)RNAseq reveal a galunisertib-driven shift toward an effector phenotype in T and NK cells characterized by a progressive downregulation in TCF1.

In summary, we demonstrate that galunisertib, a clinical stage TGF-β inhibitor, reverses SIV latency and decreases SIV reservoirs by driving T cells toward an effector phenotype, enhancing immune responses *in vivo* in absence of toxicity.

Introduction

Interruption of antiretroviral therapy (ART) leads to rapid rebound of viremia in the vast majority of people living with HIV-1 (PLWH) due to the establishment of a persistent HIV-1 reservoir early after infection[1, 2]. A key mechanism of this persistence is the ability of HIV-1 to enter a state of virological latency characterized by the silencing of viral gene expression and/or lack of viral proteins translation[3, 4]. This allows the virus to remain invisible to the immune system and latently infected cells to survive and proliferate by homeostatic or antigen-driven proliferation[5, 6]. Of note, the viral reservoir was initially thought to be stable. However, recent evidence suggests that stochastic HIV reactivation under ART occurs, and selective killing is favored in cells bearing replication competent virus integrated in transcriptionally active sites within the genome[7, 8, 9]. Hence, integration site, but especially the activation status of the infected cells profoundly influences HIV-1 persistence.

Ongoing efforts to achieve a functional cure for HIV-1 are directed towards supplementing ART with immunotherapies targeting the viral reservoir. Such strategies, under the umbrella of “shock and kill”, aim to reactivate the replication competent reservoir and eliminate latently infected cells by viral cytopathic effects or immune-mediated killing [10, 11]. However, these strategies have thus far failed to achieve a reduction of the viral reservoir or post-ART virologic control in either the clinic or preclinical models. This is mainly due to the low inducibility of latent proviruses and the heterogeneity of the mechanisms of persistence[12, 13 14, 15]. In contrast, therapeutic vaccination strategies focused on enhancing HIV/SIV-specific responses have had some discreet measure of success[16]. However, currently, no single strategy leads simultaneously to latency reversal and stimulation of effective immune responses.

The HIV life cycle and HIV’s ability to replicate efficiently are especially dependent on the activation status of the infected cells. In this context, significant advances have been made to directly activate immune cells through non-canonical pathways in order to promote HIV latency reversal[17]. However, the activation and differentiation of immune cells is intrinsically linked to cellular metabolism[18]. Indeed, signaling pathways that govern immune cell differentiation and activation such as mTOR and Wnt/β-catenin, not only have been implicated in regulating HIV latency[19, 20, 21], but are also critical regulators of cell metabolism[22]. The metabolic status of an infected cell, in turn, plays a critical role in its ability to support latency reactivation and viral production[19, 23].

In this context, recent evidence suggests that TGF-β plays a critical role in the regulation of immune cell activation and metabolic reprogramming[24, 25, 26]. Specifically, in the context of CD8$^+$ T cells, TGF-β has been shown to suppress mTOR signaling preserving the metabolic fitness of memory CD8$^+$ T cells[25] and stem-like antigen specific CD8$^+$ T cells through its modulation of Wnt/β-catenin factor TCF1[26, 27]. TCF1 and the mTOR pathway are also critical to T cell differentiation and responsible for the transition from activated effector cells to resting memory cells during LCMV infection[22, 26]. The regulation of quiescence in CD8$^+$ T cells that follows continuous TGF-β stimulation is critical to the transition to a memory phenotype and it is driven by specific metabolic changes that are linked to decreased glycolytic activity, more efficient mitochondrial respiration, and long-term survival[25, 26].

Similarly, in the context of NK cells, TGF-β has been implicated in decreasing their baseline metabolism driving lower expression of markers of NK cytotoxic activity[28].

While TGF-β-mediated suppression of TCR and IL-2 signaling were shown to lead to lower CD4$^+$ T cell activation following cognate antigen recognition in older studies[24, 29], more recent work using CD4$^+$ T cell-specific deletion of the TGF-β receptor demonstrated an even more profound effect of TGF-β on all stages of CD4$^+$ T cell activation, proliferation and cytotoxic response to LCMV than in CD8$^+$ T cells[30]. However, little is known on the specific role of TGF-β in regulating the transition to and from memory and effector phenotypes in CD4$^+$ T cells and how this may be associated with TGF-β-driven changes in CD4$^+$ T cell metabolism. Moreover, TGF-β regulates the expression of CD103 and other surface and intracellular factors essential of T cell residency in mucosal tissues[31, 32, 33]. Hence, TGF-β is considered the master regulator of mucosal immunity[34].

We and others have recently demonstrated that TGF-β regulates HIV-1 latency in primary CD4$^+$ T cells ex vivo and in vivo[35, 36, 37]. Latency reversal was detected in a non-human primate (NHP) model of HIV infection following a short treatment with a clinical stage TGF-β inhibitor, galunisertib (LY2157299)[38]. In that study, we documented latency reversal particularly at the level of the gut mucosal tissue using the ^{64}Cu-anti-gp120 Fab$_2$(7D3) probe and immuno-PET/CT[35]. We further validated the ability of immune-PET/CT to identify sites of viral reactivation and replication in the gut by performing tissue resection in hot areas of the gut identified by PET followed by confirmatory PCR for vDNA/RNA and vRNAscope[35].

Herein, we demonstrate how treatment with galunisertib with a 2-week on, 2-week off regiment that mimics the therapeutic regimen employed in the clinic in phase 1 and 2 trials of solid tumors[39, 40], leads to profound transcriptional and functional changes in immune cells in the absence of overt toxicity or increased systemic inflammation. Importantly, we observed a shift toward a transitional effector phenotype in CD4$^+$ T cells and other immune cells both systemically and in the lymph nodes. This shift was accompanied by, and likely responsible for, increased viral reactivation in SIV-infected, ART treated macaques documented by molecular techniques and PET/CT images. At the end of the treatment with galunisertib, we detected lower viral reservoir levels, including total and intact proviral DNA in both PBMC, gut and lymph nodes and significantly higher immune responses.

RESULTS

2-weeks on-off therapeutic regiment with galunisertib leads to viral reactivation SIV infected, ART-treated macaques.

To confirm galunisertib-driven HIV/SIV latency reversal and investigate the underlying mechanisms, 8 Indian origin rhesus macaques (*Macaca Mulatta*, Mamu-A01-, -B08, -B17-, all females) were infected intravenously with 300 TCID50 of the barcoded SIVmac239M2. We initiated ART treatment (daily co-formulated Tenofovir [PMPA], Emtricitabine [FTC] and

Dolutegravir [DTG]) on week 6 post-infection (pi). A 2-week on, 2-week off therapeutic cycle with galunisertib (20mg/Kg twice/daily orally) started at week ~35pi and continued for a total of 4 cycles (Fig 1A and Table S1). ART was discontinued 3 weeks after the last galunisertib dose, and the macaques were followed for 6 weeks after ART discontinuation. Median peak plasma viral load (pVL) was 10^8 copies/mL at week 2pi. Given the synergistic activity of anti-PD1 and anti-TGF-β therapies in cancer[41, 42], a rhesus anti-PD1 antibody was administered at 5mg/kg before the 3rd and 4th cycle to 2 macaques (08M156 and A6X003). However, no differences were noted for these 2 macaques in any of the parameters we measured, and the data were pooled.

Full suppression to undetectable levels (pVL LOD 15 copies/mL) was achieved in 3 out of the 8 macaques at week 10pi. In the other 5 macaques, pVL fell below 65 copies/mL by week 22pi with a single blip of 400 copies/mL in A8T010 at week 29pi (Fig 1B). Following the start of the galunisertib treatment, pVLs increased in 7 out of 8 macaques from a single peak over undetectable in 08M171 and A8L057 to several peaks and up to 10^3 copies/mL in the other macaques. Of note pVLs in A8T010 and A8R095 was undetectable for over 5 weeks before, respectively, blips of up to 10^2 copies/mL were detected following galunisertib treatment initiation (Fig 1B). More frequent blips were noted during the first 2 cycles with galunisertib compared to cycles 3 and 4 (Fig 1C). However, 08M171 and A8L057 did not experience a pVL increase until the 4th cycle.

Importantly, in support of the pVL data above, we documented viral reactivation also using immunoPET/CT. The ^{64}Cu-anti-gp120 Fab$_2$(7D3) probe was injected 24hrs before each scan and scans performed before the first and after the last galunisertib dose in each cycle. As shown in Fig 2, Fig S1 and Movies S1-S8, the PET signal visibly increased in different tissue areas after cycle 2 (in A8R095, 08M156, A8L014 and A8T010) or at the beginning of cycle 3 (in A6X003, 08M134 and A8L057). In 08M171 we observed an increase in the gut area only at the beginning of cycle 2. An unforeseen issue with probe stability in cycle 3 led to exclusion of the last 2 scans of 08M171 from the analysis (Fig S1, 08M171 infection, treatment and scan were offset compared to the other macaques). A corresponding increase in mean standard uptake values (SUV) was detected in the gastrointestinal area and axillary lymph nodes (Fig 2B) and was significant in cycle 3 compared to before cycle 1 (BC1). In these anatomical areas (ROIs in Fig S2 and Movies 9-10), SUV increases likely correspond to increases in viral replication as demonstrated in previous studies[43, 44]. A PET signal increase was also noted in the area of the vertebral column (spine) and nasal associated lymphoid tissues (NALT). However, neither cerebrospinal fluid (CSF) nor bone marrow (BM) or NALT tissue were collected during the study, and we have no prior validation of the specificity of the signal in these anatomical locations. Hence, whether this signal corresponds to increased viral replication and whether this occurs in the vertebral bones or cerebrospinal fluids remains to be determined. No SUV increase was present at the level of the spleen or kidney, where probe accumulation and background signal likely masked any specific signal. However, a significant increase in SUV was detected in the liver (Fig 2B). Similar increases in PET signal are also evident when considering the SUV Total in these anatomical areas (Fig S3A). Moreover, blood pool activity (BPA) also increased during the 3rd cycle (Fig S3B). Whether this was due to galunisertib-specific effects on probe pharmacokinetics, changes in viral antigen or probe-antigen kinetics remains to be determined. However, when the mean SUV was normalized for BPA in the gut, axillary lymph nodes and spine, the signal increase in the 3rd cycle was lost, but an increase during the first cycle became evident (Fig S3C). Of note, the non-BPA normalized SUVmean increase in the gut and lymph node areas in most cases followed an increase in cell-associated vRNA detected, respectively, in colorectal biopsies and fine needle aspirates (FNA) at the same time points during treatment (Fig S4).

Decreased viral reservoir in absence of systemic inflammation after 4 cycles with galunisertib

To determine the impact of galunsiertib on SIV reservoir, we measured CA-vDNA in PBMC, colorectal biopsies and lymph nodes (LN). A significant decrease in CA-vDNA was detected in all tissues between week 35pi (beginning of cycle 1, BC1) and week 49pi (after/end of cycle 4, AC4) for gut and LN, and between week 35pi (BC1) and end of cycle 3 (AC3) for PBMC (Fig 3A, AC4 not measured for PBMC and Fig S5A). In the gut and LN (right axillary), decreases ranged from a Log to 1/3 of a Log (gut: median 0.77; range: 0.33 - 0.94 fold LN: median: 0.93; range: 0.33-0.98 fold decrease). In the PBMC the decrease was slightly less pronounced with a median half Log decrease (median: 0.58; range 0.28 - 0.88 fold decrease). However, the comparison for the PBMCs was between week ~35 and week ~45 (end of cycle 3, AC3) instead of the end of all 4 cycles, because a snap frozen pellet was not available at the end of cycle 4 for PBMCs. The SIV reservoir in PBMCs was also monitored by SIV-IPDA (intact proviral DNA assay) comparing before cycle 1 (BC1) to the end of cycle 4 (AC4). Of note, we observed significant decreases of both total and intact provirus by SIV-IPDA. Intact provirus declined similarly to the CA-vDNA with a median of half Log (median: 0.53; range: 0-0.71 fold decrease).

In contrast, no decline in CA-vDNA was detected in the PBMCs of a group of 4 macaques infected intravenously with the same stock of SIVmac239M2 for a separate study. These 4 macaques were placed on ART on week 6pi as in our study. However, they were infected several months after our study and samples collected at similar time points varied in their availability. No decline in CA-vDNA was detected under ART, between weeks 28 and 52pi (untreated group, Fig S5B). This suggests that the decline in CA-DNA in our study was not due to ART alone. However, in absence of an appropriate control group, it is not possible to be determine with confidence the relative contribution of ART and galunisertib to the decline.

Importantly, we found no significant changes in any of the clinical variables (chemistry and hematology, Supplementary Data 1 and 2) measured before, during and after the galunisertib therapy. Moreover, we observed no changes in the concentrations of inflammatory chemokines and cytokines measured in plasma before and after the first 2 treatment cycles and at the end of the last cycle (Fig 3C). The only difference in cytokine and chemokine levels after galunisertib treatment was a small increase in IL-10 detected at the end of the last cycle compared to before treatment (Fig S5C).

Galunisertib treatment drives an effector phenotype in T and NK cells.

The phenotype of PBMCs before and after Galunisertib treatment was monitored by high-parameter flow cytometry of T and NK cell subsets and phenotype (Table S2). Classical subsets and single-color analysis of MFI revealed a substantial increase in the expression of CD95 and a profound consistent decrease in TCF1 expression in $CD4^+$ T cells that continued throughout the treatment (Fig 4A). In contrast, a small decrease in CD62L after the first cycle, reverted to baseline during the following cycles. The frequency of naïve cells, defined as $CD95^-$ within $CD4^+$ T cells, decreased in parallel with the increase in CD95 (gating strategy in Fig S6). Interestingly, there was no change in the expression of CCR7 or CD28 within $CD95^+$ $CD4^+$ T cells (Fig 4B). Hence, the frequency of central memory and effector memory as defined by CD95 and CD28 or CCR7 did not change (Supplementary Data 3). The levels of T-bet did not change significantly (Fig S7A). However, we detected a downregulation of the gut homing receptor integrin $\alpha4\beta7$ and a decrease in the levels of granzyme B (GRZB, Fig S7A). Of note, the expression of activation markers CD69, HLA-DR and Ki67 remained mostly unchanged, with the exception of an increase in HLA-DR at the beginning of cycle 2 compared to before galunisertib (Fig 4C). Interestingly, the effect of Galunisertib on $CD8^+$ T cells was not as pronounced as it was on $CD4^+$ T cells. No significant increase was detected in CD95 expression and TCF1 downregulation reached significance only at the end of the treatment (Fig 4D). Markers of cell activation like HLA-DR, Ki67 and CD69 did not change (Fig 4D and Fig S7B). However, we detected a significant decrease in T-Bet at the beginning of cycle 2 (BC2) compared to before treatment (BC1). Finally, in contrast to $CD4^+$ T cells, the decrease in GRZB was more pronounced at several time points during treatment and there was a sustained significant increase in CCR7 expression in memory $CD8^+$ T cells (Fig 4E). Interestingly, the expression of PD1 on both $CD4^+$ T cells and $CD8^+$ T cells either did not change or was slightly downregulated. Importantly, the frequency of PD1$^+$ CD101$^+$ (TCF1^{low}) exhausted memory CD8$^+$ T cells[45] did not change (Fig S7B). Finally, within NKG2A$^+$ CD8$^+$ NK cells, there was a pronounced increase in CD16 expression and an initial increase in the proliferation marker Ki67 (AC1 vs BC1; Fig 4F).

High-dimensional data visualization with tSNE and clustering analysis with FlowSOM[46] confirmed the results of the classical analysis. We performed tSNE and FlowSOM after data clean up with FlowClean and normalization with the SwiftReg algorithm[47]. We performed two analyses. One analysis compared before (BC1) and after the last cycle (AC4) only (Fig 4G and Fig S8A). A second analysis was performed on all time points (Fig S8B and S8C). When we compared only BC1 and AC4, the PhenoGraph clustering algorithm identified 36 populations. FlowSOM with 36 populations identified 6 populations of CD4$^+$ T cells, 6 of CD8$^+$ T cells and 4 of NK cells (NKG2A^{high} CD8$^+$; Fig S8A). The remaining populations were likely monocytes and other minor subsets. Direct comparison of each population revealed a decrease in Pop 31 (naïve CD8 T cells) and Pop 30 (central memory Ki67$^+$ CD8$^+$ T cells) and an increase in Pop 2 and 3 (effector and central memory CD4$^+$ T cells). Finally, there was a decrease in HLA-DR high Pop0 and an increase in CD16^{high} NKG2A$^-$ Pop14 (Fig 4H and S8A). Visual inspection of the tSNE plots (Fig 4G) revealed 3 areas mostly occupied by cells in the post-galunisertib AC4 group (New1, 2 and 3) which were characterized by high levels of CD16 and GRZB (New 3 is likely NK cells). In contrast, 3 areas mostly occupied by cells in the pre-galunisertib group BC1 (Old1, 2 and 3) were characterized by high levels of TCF1 and low CD95, confirming the finding of the classical analysis. Analysis of all time points with phenograph-derived 38 populations in FlowSOM recapitulated findings obtained with the classical analysis and the BC1 AC4 comparison with no additional insights (Fig 4I).

Galunisertib treatment in vivo increases pTreg while decreasing pTfh

The frequencies of circulating Tregs and Tfh cells were monitored with an established flow cytometry panel[48, 49] after the first and third cycle of galunisertib. The frequency of all CD4$^+$ Tregs (CD25^{high} FoxP3$^+$; gating in Fig S9) and CD8$^+$ Tregs increased after the first cycle and remained higher until the end of the 3rd cycle, while CCR4$^+$ Treg were proportionally higher at the end of the treatment compared to before (Fig 4J). In contrast, circulating Tfh (CXCR5$^+$ PD1$^+$; gating in Fig S9) were lower at the end of the Galunisertib treatment both within total and central memory CD4$^+$ T cells (Fig 4J). Finally, the expression of CD39 (ecto-nucleotide triphosphate diphosphohydrolase 1), which tracks within extracellular adenosine and immunosuppressive effects, was lower on total and central memory CD4$^+$ T cells (Supplementary Data 3 and Fig 4J, respectively).

Bulk RNAseq of PBMC and single-cell (sc)RNAseq analysis of LN confirm a profound shift toward effector phenotype.

In our previous studies, we determined that 6hrs after galunisertib treatment in naïve macaques there was an upregulation of the AP1 complex (JUN and FOS) and several genes encoding ribosomal proteins in CD4$^+$ T cells[44]. To understand early and later effect of galunisertib in the context of SIV infection, in the current study we performed bulk RNAseq of PBMC isolated 1hr after the first administration of galunisertib in cycle 1 and at the end of the 1st 2-weeks cycle. We found 640 genes significantly modulated (FDR<0.05; abs($\log_2$ FC(Fold Change))>2) in PBMC just 1hr after the first dose of galunisertib. The majority (457 genes) were downregulated (Fig 5A). Gene set enrichment analysis (GSEA) revealed an upregulation of the oxidative phosphorylation (OXPHOS; Enrichment Scores (ES) 0.58 FDR=0.048) and the reactive oxygen (ES 0.55 FDR=0.075) pathways among the Hallmark genet sets (Fig 5A and S10). Among the Biocarta sets, there was an enrichment in the electron transport chain (ETC; ES 0.84 FDR=0.132) and a downregulation of the circadian (ES -0.81 FDR=0.163) pathways (Fig 5A and S10). Finally, among the top modulated genes (by FC), we identified several genes encoding for soluble transporters, while classical activation markers like CD69 and CD38 were downregulated (Fig S10B). An early engagement of metabolic pathways was confirmed by enrichment analysis of significant DEG with Metascape[50] with an upregulation of adipogenesis, OXPHOS and fatty acid metabolism (Fig S10C). Of note, 2 weeks after the beginning of galunisertib, metabolic pathways were still among the most enriched upregulated pathways in PBMCs (Fig 5B and Fig S11A). Among the top upregulated genes there were CD44, CCR5, several integrins and GRZA and GRZB (Fig S11B). Finally, we performed bulk RNAseq of rectal biopsy tissue before and after the first cycle with galunisertib (Fig 5C). There were only 51 differentially expressed genes (DEGs; FDR<0.05; $\log_2$FC=2). GSEA analysis of all DEGs (FDR<0.05) revealed the G2_M_DNA replication pathway highly enriched (ES 0.97 FDR=0.012) within the Hallmark set. Among the most interesting changes, we observed a pronounced downregulation of integrin β7, in contrast to an increase in integrin αE (CD103; Fig 6C), suggesting that TGF-β-driven increase in αE[51] may be driven by non-canonical TGF-β pathway signaling not blocked by galunisertib.

To clarify the impact of galunisertib at the single cell level and in lymphoid tissues, we also performed scRNAseq analysis of cells isolated from LNs before (right axillar) and after (right or left inguinal) the first cycle (Fig 6). Dimensionality reduction and clustering analysis with PCA and uniform manifold approximation and projection (UMAP)[52] was performed to visualize the data (Fig 6A). However, cells were classified based only on gene expression (Fig 6B and C). We first classified major subsets: T cells (38,705 cells), B cells (31,385 cells), NK cells (1,628 cells), macrophages (285) and cells expressing both CD19 and CD3 (942 T/B cells) (Fig 6A shows this classification over UMAP). Then we classified only CD4$^+$ and CD8$^+$ T cell subsets (Fig 6C and S12A) and B/T subsets including naïve and germinal center (GC) B cells and Tfh cells (Fig S12B and S12C). Cell number for all these subsets did not change with treatment (Fig S13). However, differential gene expression analysis of T cells revealed an upregulation of members of the AP1 complex, CD69, β2 macroglobulin and RPL13 among the most upregulated genes (Fig 6D). Moreover, it confirmed a downregulation of TCF1 at the transcriptional level (*TCF7* gene; Fig 6D). Gene enrichment analysis revealed again Myc_targets_V1, OXPHOS and mTORC1 as the most enriched hallmark pathways (Fig 6E). Of note, among gene ontology cellular processes, RNA processing was the most highly enriched pathway, followed by intracellular transport and catabolic processes following right after (Fig S14A) confirming an increase in translation and metabolism within these cells.

Since we noticed substantial differences in the impact of galunisertib on CD4$^+$ T cells compared to CD8$^+$ T cells by flow, we focused the analysis on these subsets. In CD4$^+$ T cells we found only 25 DEGs with a $\log_2$FC=0.15, while 34 DEGs were in CD8$^+$ T cells with more downregulated genes in the CD8$^+$ T cells compared to the CD4$^+$ T cells. The AP1 complex and *TCF7* were again upregulated and downregulated respectively in both CD4$^+$ (Fig 6F) and CD8$^+$ T cells (Fig 6G). However, STAT1 was more strongly downregulated in CD4$^+$ T cells. Enrichment analysis showed once again upregulation of Myc_targets_V1, OXPHOS and mTORC1 pathways in both CD4$^+$ and CD8$^+$ T cells (Fig 6H and Fig S14B). Interestingly, the most enriched set among in Biocarta was the HIV-Nef pathway (Fig 6I) demonstrating the relevance of these galunisertib-driven changes to HIV cell cycle and transcription (highly enriched KREB pathway as well). The 2nd most enriched Biocarta pathway was TCR signaling, linking galunisertib to cell activation. Next, we analyzed changes in gene expression in Tfh cells. In this subset we obtained a similar number of DEG as in other T cells and myc_targets_V1 was still the most enriched hallmark pathway (Fig S14C and D). In B cells, the AP1 complex was again prominently upregulated, together with CD83, CD69 and MAMU-DR. Of note, more genes were modulated in B cells (44 genes with a $\log_2$FC=0.15 and 18 with logFC0.2) than in T cells with some differences in enriched pathways (Fig S14F). Similar genes were modulated in GC B cells and naïve B cells with several more DEGs in naïve B cells than in GC cells (Fig S15A and B). Finally, 144 genes were modulated in NK cells and 39 genes in macrophages (Fig S15C and D; $\log_2$FC=0.15). GRZB was prominently upregulated, but

CD44 downregulated. In macrophages genes were mostly downregulated including TCF7L2 and KLF4 suggesting an increase in inflammatory phenotype and decrease in M2 polarization[53] (Fig S15D).

Galunisertib increases SIV-specific responses and changes barcode distribution

In order to understand how galunisertib affected immune cell function and SIV-specific responses, we stimulated PBMC with 15-mer SIV peptides from SIVmac239 gag, pol and env for 24hrs on antibody coated Elispot plates. Because of sample availability, we probed before and after the first cycle and after the 3rd galunisertib cycle only. Interestingly, by the end of the 3rd cycle there was a significant increase in IFN-γ secretion both SIV-specific (particularly against env) and non-specific (DMSO control). A notable increase in TNF-α release was similar in response to Gag and non-specifically (Fig 7). In contrast, IL-2 release appeared to increase slightly after the first cycle (non-significant), but remained unchanged with a slight decrease by the end of the 3rd cycle (Fig 7).

In order to understand if these changes in immune responses in combination with latency reversal and switch toward an effector phenotype may have impacted viral population dynamics, we analyzed changes in numbers and distribution of the viral barcodes before and after the first 3 treatment cycles. There was no barcode amplification at several time points particularly in the lymph nodes. However, although there were no significant changes in the number or diversity (measured as Shannon Entropy; Sh) of barcodes before and after each galunisertib cycle (Fig S16A and Fig 8A), we found significant changes in barcode frequency distribution in most tissues and cycles after galunisertib treatment (Fig 8B and S16B). Specifically, the relative proportion of each barcode changed in all monkeys in all cycles in the rectal biopsies (probably a consequence of different sampling area), but also for all LN analyzed (except for 08M134 in cycle 1). Of note, the same LN were sampled at the beginning and after cycle 3 (Table S3). Hence, sampling location does not explain the changes barcode distribution. Changes in the proportion of barcodes were also detected in at least half of the PBMCs after cycle 1 and 2 (cycle 3 not analyzed). Finally, barcode diversity decreased in plasma post-ATI compared to the time point right before ART (Fig 8C) and barcode distribution significantly changed post-ATI compared to pre-ART in 2 of the 7 macaques that rebounded (Fig S16C).

TCF1 downregulation in CD4$^+$ T cells correlates with virological and immunological endpoints.

In order to explore a possible association between the various virological and immunological parameters and their changes, we built a correlation matrix with a curated set of variables of interest or their fold changes. This analysis revealed an association between the decrease in TCF1 expression in the CD4$^+$ T cells and several virological and immunological variables (Fig 8E). Specifically, both the levels of CA-vDNA in the colorectal tissue and the fold increase in gut-SUV strongly inversely correlated with fold changes in TCF1. Since TCF1 decreased, a larger decrease in TCF1 was directly proportional to residual vDNA in the gut at the end of cycle 4 and to the increase in PET signal in the gut (Fig 8D and 8E). A weaker, but still significant association was also present with CA-vDNA in PBMC at the end of cycle 3 and with the levels of vRNA in the lymph nodes at the end of the 4th cycle (Fig 8D and S17A). Finally, the decrease in TCF1 correlated with the increase in IFN-γ and poly-functional IFN-γ/TNF-α releasing cells (cumulative increase of SIV-specific responses to gag, pol and env; Fig 8D and 8E). Of note, the increase in PET signal in the gut also correlated with the levels of vDNA in PBMC at the end of cycle 3, vDNA in gut biopsies and residual CA-vRNA in LN at the end of cycle 4 (Fig S17B). Interestingly, the levels of residual CA-vRNA in LN also correlated with the increase in IFN-γ and poly-functional IFN-γ/TNF-α releasing cells (Pearson r=0.85 and 0.76, respectively). Finally, the residual intact pro-virus (IPDA) directly correlated with the levels of IFN-γ and IFN-γ/TNF-α produced in response to SIV peptides at the end of cycle 3 (Fig 8D; r= 0.76 and 0.88, respectively). In contrast, the change in intact provirus trented to correlate inversely with the levels of IFN-γ, so that a larger decrease directly correlated with more IFN$-\gamma$ responses. However, this did not reach significance (p=0.117, Fig S17C).

Discussion

HIV-1 latency in T cells is maintained through diverse mechanisms that include blocks in transcriptional elongation, completion, and splicing[13]. A common characteristic shared by HIV-1 latently infected cells of both T and myeloid cell lineages is their "resting" phenotype[14, 54, 55, 56] In these cells, an inability to transcribe proviral DNA is linked to a generalized decrease in transcriptional activity which, in turn, is linked to their metabolic status[23]. Cellular metabolism is in turn influenced by tissue location and environmental cues[57].

TGF-β is released at high level in PLWH and its levels remain high during ART[58, 59, 60]. The immunosuppressive activity of TGF-β is well-known. However, the effect of TGF-β signaling in immune cells is highly context dependent[61]. Hence, TGF-β plays different roles according to a cell differentiation and activation status[61]. In CD8$^+$ T cells and NK cells, TGF-β was shown to decrease mTOR activity and preserve cellular metabolism (high mitochondrial activity and spare respiratory capacity, but reduced mTOR activity) preventing metabolic exhaustion[25, 26, 62, 63]. This effect was linked to survival of antigen-specific CD8$^+$ T cells, preservation of their stemness and it was linked to higher expression of the TCF1 factor[25].

In contrast, in CD4$^+$ T cells TGF-β is known to decrease TCR activation[29, 64], restrict proliferation and inhibit cytotoxicity (including granzyme and perforin release) at different stage of infection in vivo[30, 65]. However, the role of TGF-β in the formation and preservation of CD4$^+$ T cell memory is still unclear[61]. Moreover, the link between TGF-β signaling and TCF1 expression in CD4$^+$ T cells is unexplored.

Here, we used a clinical stage small drug, galunisertib, developed by Eli Lilly and used in several phase 1 and 1/2 clinical studies against solid cancer[39, 66, 67] to investigate the impact of TGF-β blockade on SIV latency, SIV reservoir and immune responses. Of note, Eli Lilly did not terminate galunisertib development program because of toxicity[68, 69]. Indeed, in our studies in macaques, we observed no adverse events nor changes in chemical or hematological variables. Moreover, there were no detectable changes in the levels of the 24 inflammatory factors that we probed in plasma during the treatment. This suggests that this therapeutic approach may be safe in people living with HIV (PLWH).

The first important finding of our study was the confirmation of our previous report of the latency reversal properties of TGF-β blockade in vivo[35]. Indeed, we found increase in pVL in 7 out of the 8 macaques upon initiation of galunisertib therapy. Although not all macaques were fully suppressed before treatment, substantial increases in pVL (>10^2 copies/mL) were noted also in fully suppressed macaques (08M171, A8R095 and A8L057). Moreover, viral reactivation was documented in tissues by immunoPET/CT. Importantly, the SUV increase detected post-galunisertib in gut and LN correlated with CA-vRNA as in our previous studies[35] and, interestingly, it was associated with a decrease in TCF1. However, despite this evidence, the absence of imaging studies carried out in uninfected, galunisertib-treated macaques require that we interpret this data with care. This is due mostly to unexpected and, yet unexplained, galunisertib-driven changes in BPA. Without a better understanding of these changes, it is difficult to determine the BPA contribution to the PET signal increase in tissues. Yet, an increase in gut and LN SUV is present even after BPA normalization (although in cycle 1 instead than cycle 3). Since our probe is a $F(ab')_2$ and not a whole antibody, we did not expect the probe to be still present in significant amounts in circulation in a scan performed 24hrs post-probe injection. Nonetheless, galunisertib may have impacted probe and probe-antigen complex pharmacokinetics or the probe interaction with increased viral antigen. TGF-β is required for vascular barrier function[70]. Hence, galunisertib may have increased vascular permeability. However, this would have driven a major decrease in

BPA instead than the detected increase. Moreover, significant changes in VEGF-A, a factor critical to and tracking with vascular permeability[71], were not noted. This, in conjunction with our previous studies which validated the specificity of the PET signal for areas of enhanced SIV replication in gut and lymph nodes[35, 43, 72], demonstrates that the galunisertib-driven increases in SUV were likely specific, and identified areas of SIV latency reversal at least in gut and lymphoid tissues. The extent to which the increased signal in the spine and bones recapitulates an increase in SIV replication at these sites remains to be determined.

Importantly, we observed a decrease in CA-vDNA in all the tissues that cannot be attributed to ART alone. Indeed, although we did not have a concurrent control group, this decrease was not present in similar studies conducted in SIVmac239M2 infected macaques on the same ART regimen, but not treated with galunisertib. Considering studies by other groups with different models (SIVmac251), they report 2nd phase decay of SIV intact provirus (weeks ~32 to ~100pi, Fig 2B in[73]) with a $t_{1/2}$ of >8 months[73]. In contrast, in our study, the intact provirus decreased by 3 fold (median) in a little over 3 months (from week 35pi, BC1 to week 49pi, AC4). Interestingly, this decrease in intact pro-virus trended toward a direct correlation with IFN-γ responses. However, IFN–γ levels also inversely correlated with the absolute value of residual intact provirus, suggesting that IFN-γ responses were driven by residual viral reservoir while, at the same time, were involved in clearing intact virus. Indeed, the increase in IFN-γ and TNF-α also correlated with residual CA-vRNA in the LN at the end of the treatment. The latter, in turn, was directly proportional to the increase in gut SUV. This is in line with increased latency reversal explaining residual viral RNA in lymphoid tissues.

Finally, one of our most intriguing results was the profound downregulation of TCF1 in CD4$^+$ T cells at both the transcriptional and protein levels. Although TCF1 is conventionally viewed as an effector of the canonical Wnt pathway[74] and recently reached notoriety for its role in maintaining stemness of antigen-specific memory CD8$^+$ T cells[26, 75], TCF1 has a plethora of functions in T cell development and differentiation largely independent of Wnt signaling[22]. In CD4$^+$ T cells, TCF1 has been implicated in orchestrating all the major Th subsets, including Th1, Th2, Th17 and Tfh[76]. TCF1 is known to control the bifurcation between Th1 and Tfh in favor of Tfh cells[76], while it negatively regulates Treg development[22]. This is in line with our findings of increased Treg and decreased Tfh, in the midst of a profound downregulation of TCF1. Importantly, TCF1 is downregulated with increased cellular differentiation and progression toward effector functions in T cells. T cell activation leads to reduced levels of TCF1 and higher levels of TCF1 are present in T cells with higher stemness and low anabolic metabolism[74]. These findings suggest that TCF1 has a critical role in maintaining quiescence in immune cells likely in concert with TGF-β[18, 65]. Our data reveal that this link may be even more prominent and important in CD4$^+$ T cells than in CD8$^+$ T cells. Importantly, the decrease in TCF1 was accompanied with enhancement in other effector markers such as CD95, CD16 and GRZB (at the transcriptional level) and an increase in the transcription of AP1 complex. However, there was no clear upregulation of other classical markers of immune activation such as CD69 and no increase in T cell proliferation (Ki67 expression). Hence, galunisertib treatment does not appear to lead to classical T cell activation nor to an increase in a specific terminally differentiated effector subset. Instead, in vivo TGF-β blockade seems to primarily change the metabolic state of T cells (and likely other immune cells) increasing OXPHOS and mitochondrial function. Of note, although glycolysis is essential during cell activation, mitochondrial pathways are engaged and remodeled early after activation and OXPHOS upregulation has a pivotal role in the earliest stages of cell activation[18].

Hence, we propose a model in which TGF-β inhibition forces cells (particularly CD4$^+$ T cells) out of quiescence to a transitional state where they reinitiate their transcriptional program and are metabolically ready to be activated. Because of the highly context-dependent effect of TGF-β, the final impact of galunisertib is likely heterogenous and dependent on other intrinsic and extrinsic cellular stimuli. In absence of direct TCR engagement or other activation stimuli, the majority of the T cells does not undergo full/classical activation and proliferation following galunisertib treatment. Instead, the cells are pushed toward a more effector-like phenotype. This explains our observation of an enrichment of transient effector or “transitional effector” T cells that, in turn, can reinitiate viral transcription and more promptly respond to antigenic stimulation. Indeed, functionally, we demonstrated that the PBMC after galunisertib treatment secrete higher levels of IFN-γ and TNF-α. Interestingly, there was no increase in IL-2 secretion. The link between TGF-β and IL-2[77] and the critical role of IL-2 in T cell proliferation again suggest that galunisertib enhances an effector phenotype uncoupled from cellular proliferation. scRNAseq analysis demonstrated a trend toward an effector phenotype also in other immune cells, such as B cells, NKs and macrophages. Future studies will need to uncover in depth the effect of TGF-β blockade on these other immune subsets.

This study has several limitations. The most important limitations are the relatively small number of macaques and the lack of a concurrent untreated control group. We also could not investigate in depth the viral kinetics after ART interruption because of the short follow up after ATI. An additional important limitation is the lack of immunoPET/CT images from an uninfected control group of macaques treated with galunisertib. This control group may have given us insight on the impact of galunisertib on the pharmacokinetics of the immunoPET/CT probe in absence of antigen. Moreover, we did not explore changes in the phenotype or turnover of cells isolated from gut and lymph nodes and relied solely on transcriptional data for these tissues. Although we found an association between TCF-1 downregulation, enhanced effector function (IFN-γ release) and measures of latency reversal, a causal link between increased effector phenotype and latency reversal was not definitively established. Finally, because of sample availability, we could not dissect the cellular origin of increased IFN-γ and TNF-α.

In conclusion, we report that in vivo treatment with a clinical stage small molecule TGF-β inhibitor drives a transitional effector phenotype in T cells that is likely responsible for increasing the frequency of spontaneous latency reversal events, stimulating SIV-specific immune responses, and decreasing the viral reservoir. Future work will determine whether the galunisertib-driven enhanced antiviral responses and decreased viral reservoirs can significantly contribute to post-ART virological control.

METHODS

Study design and Ethics Statement

A total of 8 adult female Indian origin *Rhesus* macaques (*Macaca mulatta*; Mamu A*01, B*08 and B*17 negative) were used for the study described in the manuscript (Table S1). All the macaques were selected form the colonies bred and raised at the New Iberia Research Center (NIRC), University of Louisiana at Lafayette. All animal experiments were conducted following guidelines established by the Animal Welfare Act and the NIH for housing and care of laboratory animals and performed in accordance with institutional regulations after review and approval by the Institutional Animal Care and Usage Committees (IACUC) of the University of Louisiana at Lafayette (2021-8821-002; protocol 8821-01).

Rhesus macaques (n=8 main study + 4 separate non-concomitant study) were infected with 300 $TCID_{50}$ of the barcoded SIVmac239M2 stock intravenously and ART (Tenofovir [PMPA] at 20mg/ml, Emtricitabine [FTC] at 40mg/ml and Dolutegravir [DTG] at 2.5mg/ml) was initiated on week 6 pi. Galunisertib treatment was initiated on week 35 p.i. Powder (MedChemExpress – MCE, NJ, USA) was dissolved in water and given orally in a treat twice daily at 20mg/kg. 4 cycles of 2 weeks daily treatment with 2 weeks wash out period were performed. Macaques 08M156 and A6X003 were given the rhesus recombinant antibody (rhesus/human chimeric) anti-PD1 antibody [NIVOR4LALA; comprising silenced rhesus IgG4k constant regions and variable regions from anti-human PD-1, nivolumab; non-human primates reagents resource, NHPRR; 5mg/kg] at the beginning of the 3rd and 4th galunisertib cycle.

Blood viral load was monitored biweekly before and during ART and every 3-4 days during Galunisertib treatment. Colorectal biopsies and LN FNA were collected before and after galunisertib treatment. ART was terminated 3 weeks after the last galunisertib dose and euthanasia and necropsy to harvest tissues were performed at week 58 post infection, tissues samples were flash frozen, fixed in OCT or Z-fix.

Plasma and Tissue SIV Viral loads (VL)

Blood was collected in EDTA tubes and plasma was separated by density gradient centrifugation and used for the determination of plasma VL by SIVgag qRT-PCR at NIRC or at Leidos (Quantitative Molecular Diagnostics Core, AIDS and Cancer Virus Program Frederick National Laboratory). Tissue VL from snap frozen PBMC pellets, colorectal biopsies and LN FNA were performed as described in [78]. Briefly, tissue viral DNA and RNA loads were measured, respectively, by qPCR and qRT-PCR with standard curve method and normalized on Albumin copy number (for cell-associated viral DNA) and total RNA quantity. DNA and RNA were extracted from snap frozen tissues using DNeasy/RNeasy blood and tissue kits (Qiagen) following the manufacturer’s instructions. Primers: SIVgag FW (5’-GGTTGCACCCCCTATGACAT-3’), SIVgag RV (5’-TGCATAGCCGCTTGATGGT-3’), SIVProbe (5’-6-FAM-AATCAGATGTTAAATTGTGTGGGA-3’); macaque Albumin FW (5’-ATTTTCAGCTTCGCGTCTTTTG-3’), RV (5’-TTCTCGCTTACTGGCGTTTTCT-3’), Probe: (5’-6-FAM-CCTGTTCTTTAGCTGTCCGTG-3’. SIV-IPDA was performed on freshly stored PBMC before cycle 1 and at the end of cycle 4 of galunisertib by Accelevir, Baltimore, MD.

ImmunoPET/CT

ImmunoPET/CT for mapping SIV signals in total body scans were conducted in part as reported [44]. The probe consisted of primatized p7D3 anti-env F(ab)’2 coupled with the chelator DOTA and labeled with Cu^{64} just prior to administration to the animals. For probe administration, the animals were sedated, and a venous catheter was placed into an arm of leg vein to minimize bleeding of the probe into the tissue surrounding the site of injection. The probe for each animal consisted of

~1mg of the p7D3 F(ab)'2 labeled with 2-3 mCi of ^{64}Cu. After injection, the animals were allowed to recuperate in their cage until the next day. At 24 hours, the animals were again anesthetized with Telazol and the macaque's body was immobilized in dorsal recumbency on the scanner table. Scans were conducted in a Phillips Gemini TF64 scanner. The final CT image was compiled from 200 to 300 slices, depending on macaque size.

PET Image analysis was performed using the MIM software. PET/CT fusions were generated scaled according to calculated Standardized Uptake Values (SUV). The SUV scale for the PET scans was selected based on the overall signal intensity of the PET scans (whole body), and the CT scale was selected for optimal visibility of the tissues. All images and maximum image projections (MIP) were set to the same0-1.5 scale for visual comparisons. Additional details on MIM analysis are described in Supplemental Methods.

Cell isolation, flow cytometry staining, classical and high-dimensional analysis

Colorectal biopsy tissues were isolated by enzymatic digestion while LN biopsies were passed through a 70μm cell strainer as described in[44]. Isolated cells were phenotyped with panels listed in Supplemental Table S2. FlowJo vs 10.8 was use for both classical and high-dimesional analysis. PeacoQC, FlowtSNE and FlowSOM plug-ins were used with default settings. SwiftReg was used for normalization[47]. More details on the staining procedures and analysis pipeline in Supplemental Methods.

Bulk and scRNAseq analysis

For bulk RNAseq, snap frozen PBMC pellets from BC1, 1hr after first Gal dose and AC1 were used for RNA extraction with the RNeasy kit with on column DNA digestion (Qiagen). Library preparation was performed using TruSeq Stranded Total RNA with Ribo-Zero Globin and sequencing was done with an Illumina HiSeq4000 with >20M reads/samples. Sequencing data was demultiplexed and trimmed using Trimmomatic v0.36 to remove adapters and low-quality reads. Trimmed reads were aligned to the Mmul10 reference genome and transcripts quantified using the Hisat2-StringTie pipeline[79]. Differential gene expression analysis using the quantified gene transcripts was performed with DESeq2 R package[80] comparing the samples attained before and after galunisertib treatment and controlling for intra-animal autocorrelation. Differentially expressed genes (DEGs) were analyzed by functional enrichment analysis and gene set enrichment analysis (GSEA) to identify specific pathways and molecular processes altered by galunisertib.

The Parse pipeline and Partek software were used for scRNAseq analysis. For bulk RNAseq features with <100 counts were removed, data normalized and DESeq2 was used to obtain a DEG list. Genes with a false discovery rate (FDR)-adjusted p-value ≤0.05 and absolute $\log_2$ fold-change (FC) (compared to BC1) above 2 were defined as significantly differentially expressed (DEG). For scRNAseq analysis cells isolated from lymph nodes before (BC1) and after (AC1) galunisertib were fixed with the Parse fixation kit, barcoded and sequenced at the NUseq Core. The Partek software was used for scRNAseq analysis. Cells with 400-8000 features, excluding features with 0 reads in >99.99 cells, were included. Scran deconvolution was used for normalization and cell classification was based on gene expression. Hurdle models were used to compare DEGs in each cell subset before and after galunisertib. See supplemental methods for a detailed description of scRNAseq analysis and additional control analysis using Seurat R package with more stringent QC cut-offs and SCTransform normalization.

Plasma cytokines and T cell responses

Cytokines in plasma (at 1:2 dilution) were measured using the NHP Cytokine 24-Plex kit by Meso Scale Diagnostics (MSD) according to manufacturer instructions. Frozen PBMC collected at week 6 post-infection (pre-ART), right before the first galunisertib administration (BC1), at the end of cycle 1 (AC1) and at the end of cycle 3 (AC3) were thawed in AIM V medium (Thermo Fisher) with benzonase (Sigma) and plated on a FluoroSpot (CTL) plate pre-activated with 70% Ethanol and IFN-γ, TNF-α and IL-2 capture solution. Gag, pol, and env 15-mer peptides (NIH AIDS Reagents program) were prepared at two times the final concentration of 2.5µg/mL with co-stimulatory reagents anti-CD28 10µg/mL and anti-CD49d 10µg/mL and added to the cells in CTL-Test^{TM} Medium. Parallel positive control of PMA (20ng/mL) and ionomycin (200ng/mL) or mock DMSO solution was also plated with the stimulatory reagents. PBMCs were added at 300,000 cells per well. After 24hrs, the plate was washed, and incubated with detection and tertiary solutions and shipped to CTL for scanning and QC.

Statistics

GraphPad Prism v10, R and Python were used for statistical analysis and data visualization. Wilcoxon matched-pairs test and repeated measures ANOVA or mixed effect analysis (when the data set had missing data) were used to compare the different virological and immunological variables between baseline (BC1) and a single or multiple post-galunisertib time points. In Prism the mixed model uses a compound symmetry covariance matrix, and is fit using Restricted Maximum Likelihood (REML). Cytokine data from MSD assay were first Log transformed, then normalized by subcolumn/factor in percentage with 0% as smallest value and 100% larger value in each dataset. Each factor was analyzed separately with ANOVA for repeated measures and Dunn's multiple comparison's post-hoc test and together by principal component analysis (PCA). Holm-Sidak test was used for multiple comparison correction in all cases, but FlowSOM cluster comparison where the FDR method was used. Pearson r coefficient was calculated for pairwise tests of association in a correlation matrix with selected variables. For RNAseq analysis see above and supplemental methods. For viral population analysis, Shannon Entropy of the viral barcodes present in each sample was used to measure the diversity of the viral populations (see supplemental Methods). Chi-squared tests were used in R to compare barcode composition between before and after cycle time points within a tissue/macaque using paired barcode relative frequencies. Unless otherwise specified p-value<0.05 was considered statistically significant.

Data Availability Statement

All relevant data are included in the manuscript or supplemental material. Source data are provided with this paper in the Source Data file. Raw data files including DICOM image files are available to be shared upon request to the corresponding author elena.martinelli@northwestern.edu. All RNA sequencing data originating from this study have been deposited in NCBI GEO under the accession code: GSE244871.

Acknowledgements

General: We acknowledge the helpful staff at the New Iberia Research Center as well as the help of Dr. Suchitra Swaminathan and the rest of the staff of the Flow Cytometry Core Facility at the Robert H. Lurie Comprehensive Cancer Center of Northwestern University in Chicago. Moreover, we thank the staff of the NUseq Core at Northwestern, and in particular Dr. Ching Man Wai and Matthew Schipma for the help with RNAseq data. Finally, we thank Dr. Lifson and the Leidos staff for viral load measurements as well as Dr. Laird at Accelevir for providing SIV-TILDA results in a timely manner. The content of this publication does not necessarily reflect the views or policies of the Department of Health and Human Services, nor does mention of trade names, commercial products, or organizations imply endorsement by the U.S. Government.

Funding: This project has been funded by National Institutes of Health grant R56AI157822 and R01AI-176599 to Dr. Martinelli, the resource for NHP immune reagents to Dr. Villinger (R24 OD010947) for probe productions and in part with federal funds from the National Cancer Institute, National Institutes of Health, under Contract No. 75N91019D00024/HHSN261201500003I. The Lurie Cancer Center is supported in part by an NCI Cancer Center Support Grant #P30 CA060553.

Authors contributions: EM conceptualized the studies; JK performed and analyzed flow cytometry and immunePET/CT data; DB, MA, DF and SA collected and processed macaque samples; MRH generated vRNA/DNA and Elispot data; RC and MV analyzed Treg/Tfh; YT and TJH contributed to immunePET/CT analysis; EG, YG and EM analyzed RNAseq data; CMF, BK and RLR analyzed barcode data; JA, CC, FV and EM interpreted the data and wrote the manuscript.

Competing interests: The corresponding author's institution, Northwestern University filed a patent application including all the data from the present manuscript. Application number:

18/515,196, Filing date: November 20, 2023. Inventor, Elena Martinelli. All other authors declare no competing interests.

REFERENCES

1. Gantner P, *et al.* HIV rapidly targets a diverse pool of CD4(+) T cells to establish productive and latent infections. *Immunity* **56**, 653-668 e655 (2023).

2. Whitney JB, *et al.* Rapid seeding of the viral reservoir prior to SIV viraemia in rhesus monkeys. *Nature* **512**, 74-77 (2014).

3. Persaud D, Zhou Y, Siliciano JM, Siliciano RF. Latency in human immunodeficiency virus type 1 infection: no easy answers. *J Virol* **77**, 1659-1665 (2003).

4. Margolis DM, Archin NM. Proviral Latency, Persistent Human Immunodeficiency Virus Infection, and the Development of Latency Reversing Agents. *The Journal of infectious diseases* **215**, S111-S118 (2017).

5. Wagner TA, *et al.* HIV latency. Proliferation of cells with HIV integrated into cancer genes contributes to persistent infection. *Science* **345**, 570-573 (2014).

6. Maldarelli F, *et al.* HIV latency. Specific HIV integration sites are linked to clonal expansion and persistence of infected cells. *Science* **345**, 179-183 (2014).

7. Cohn LB, *et al.* HIV-1 integration landscape during latent and active infection. *Cell* **160**, 420-432 (2015).

8. Einkauf KB, *et al.* Parallel analysis of transcription, integration, and sequence of single HIV-1 proviruses. *Cell* **185**, 266-282 e215 (2022).

9. Lian X, *et al.* Progressive transformation of the HIV-1 reservoir cell profile over two decades of antiviral therapy. *Cell Host Microbe* **31**, 83-96 e85 (2023).

10. Singh V, Dashti A, Mavigner M, Chahroudi A. Latency Reversal 2.0: Giving the Immune System a Seat at the Table. *Curr HIV/AIDS Rep* **18**, 117-127 (2021).

11. Abner E, Jordan A. HIV "shock and kill" therapy: In need of revision. *Antiviral Res* **166**, 19-34 (2019).

12. Ait-Ammar A, *et al.* Current Status of Latency Reversing Agents Facing the Heterogeneity of HIV-1 Cellular and Tissue Reservoirs. *Frontiers in microbiology* **10**, 3060 (2019).

13. Yukl SA, *et al.* HIV latency in isolated patient CD4(+) T cells may be due to blocks in HIV transcriptional elongation, completion, and splicing. *Sci Transl Med* **10**, (2018).

14. Siliciano JD, Siliciano RF. Low Inducibility of Latent Human Immunodeficiency Virus Type 1 Proviruses as a Major Barrier to Cure. *J Infect Dis* **223**, 13-21 (2021).

15. Ho YC*, et al.* Replication-competent noninduced proviruses in the latent reservoir increase barrier to HIV-1 cure. *Cell* **155**, 540-551 (2013).

16. Borducchi EN*, et al.* Ad26/MVA therapeutic vaccination with TLR7 stimulation in SIV-infected rhesus monkeys. *Nature* **540**, 284-287 (2016).

17. Nixon CC*, et al.* Systemic HIV and SIV latency reversal via non-canonical NF-kappaB signalling in vivo. *Nature* **578**, 160-165 (2020).

18. O'Sullivan D. The metabolic spectrum of memory T cells. *Immunol Cell Biol* **97**, 636-646 (2019).

19. Crater JM, Nixon DF, Furler O'Brien RL. HIV-1 replication and latency are balanced by mTOR-driven cell metabolism. *Front Cell Infect Microbiol* **12**, 1068436 (2022).

20. Besnard E*, et al.* The mTOR Complex Controls HIV Latency. *Cell Host Microbe* **20**, 785-797 (2016).

21. Barbian HJ*, et al.* beta-catenin regulates HIV latency and modulates HIV reactivation. *PLoS Pathog* **18**, e1010354 (2022).

22. Gounari F, Khazaie K. TCF-1: a maverick in T cell development and function. *Nat Immunol* **23**, 671-678 (2022).

23. Valle-Casuso JC*, et al.* Cellular Metabolism Is a Major Determinant of HIV-1 Reservoir Seeding in CD4(+) T Cells and Offers an Opportunity to Tackle Infection. *Cell Metab* **29**, 611-626 e615 (2019).

24. Oh SA, Li MO. TGF-beta: guardian of T cell function. *Journal of immunology* **191**, 3973-3979 (2013).

25. Gabriel SS*, et al.* Transforming growth factor-beta-regulated mTOR activity preserves cellular metabolism to maintain long-term T cell responses in chronic infection. *Immunity* **54**, 1698-1714 e1695 (2021).

26. Hu Y*, et al.* TGF-beta regulates the stem-like state of PD-1+ TCF-1+ virus-specific CD8 T cells during chronic infection. *J Exp Med* **219**, (2022).

27. Ma C, Zhang N. Transforming growth factor-beta signaling is constantly shaping memory T-cell population. *Proc Natl Acad Sci U S A* **112**, 11013-11017 (2015).

28. Viel S*, et al.* TGF-beta inhibits the activation and functions of NK cells by repressing the mTOR pathway. *Sci Signal* **9**, ra19 (2016).

29. Delisle JS*, et al.* The TGF-beta-Smad3 pathway inhibits CD28-dependent cell growth and proliferation of CD4 T cells. *Genes Immun* **14**, 115-126 (2013).

30. Lewis GM, Wehrens EJ, Labarta-Bajo L, Streeck H, Zuniga EI. TGF-beta receptor maintains CD4 T helper cell identity during chronic viral infections. *J Clin Invest* **126**, 3799-3813 (2016).

31. Nath AP*, et al.* Comparative analysis reveals a role for TGF-beta in shaping the residency-related transcriptional signature in tissue-resident memory CD8+ T cells. *PLoS One* **14**, e0210495 (2019).

32. Zhang N, Bevan MJ. Transforming growth factor-beta signaling controls the formation and maintenance of gut-resident memory T cells by regulating migration and retention. *Immunity* **39**, 687-696 (2013).

33. Hirai T*, et al.* Competition for Active TGFbeta Cytokine Allows for Selective Retention of Antigen-Specific Tissue- Resident Memory T Cells in the Epidermal Niche. *Immunity* **54**, 84-98 e85 (2021).

34. Larson C*, et al.* TGF-beta: a master immune regulator. *Expert Opin Ther Targets* **24**, 427-438 (2020).

35. Samer S*, et al.* Blockade of TGF-beta signaling reactivates HIV-1/SIV reservoirs and immune responses in vivo. *JCI Insight* **7**, (2022).

36. Bergstresser S, Kulpa DA. TGF-beta Signaling Supports HIV Latency in a Memory CD4+ T Cell Based In Vitro Model. *Methods Mol Biol* **2407**, 69-79 (2022).

37. Chinnapaiyan S, Dutta RK, Nair M, Chand HS, Rahman I, Unwalla HJ. TGF-beta1 increases viral burden and promotes HIV-1 latency in primary differentiated human bronchial epithelial cells. *Scientific reports* **9**, 12552 (2019).

38. Holmgaard RB*, et al.* Targeting the TGFbeta pathway with galunisertib, a TGFbetaRI small molecule inhibitor, promotes anti-tumor immunity leading to durable, complete responses, as monotherapy and in combination with checkpoint blockade. *J Immunother Cancer* **6**, 47 (2018).

39. Melisi D*, et al.* Safety and activity of the TGFbeta receptor I kinase inhibitor galunisertib plus the anti-PD-L1 antibody durvalumab in metastatic pancreatic cancer. *J Immunother Cancer* **9**, (2021).

40. Wick A*, et al.* Phase 1b/2a study of galunisertib, a small molecule inhibitor of transforming growth factor-beta receptor I, in combination with standard temozolomide-based

radiochemotherapy in patients with newly diagnosed malignant glioma. *Invest New Drugs* **38**, 1570-1579 (2020).

41. Martin CJ*, et al.* Selective inhibition of TGFbeta1 activation overcomes primary resistance to checkpoint blockade therapy by altering tumor immune landscape. *Sci Transl Med* **12**, (2020).

42. Terabe M*, et al.* Blockade of only TGF-beta 1 and 2 is sufficient to enhance the efficacy of vaccine and PD-1 checkpoint blockade immunotherapy. *Oncoimmunology* **6**, e1308616 (2017).

43. Santangelo PJ*, et al.* Whole-body immunoPET reveals active SIV dynamics in viremic and antiretroviral therapy-treated macaques. *Nat Methods* **12**, 427-432 (2015).

44. Samer S*, et al.* Blockade of TGF-β signaling reactivates HIV-1/SIV reservoirs and immune responses in vivo. *bioRxiv*, 2022.2005.2013.489595 (2022).

45. Im SJ, Konieczny BT, Hudson WH, Masopust D, Ahmed R. PD-1+ stemlike CD8 T cells are resident in lymphoid tissues during persistent LCMV infection. *Proc Natl Acad Sci U S A* **117**, 4292-4299 (2020).

46. Van Gassen S*, et al.* FlowSOM: Using self-organizing maps for visualization and interpretation of cytometry data. *Cytometry A* **87**, 636-645 (2015).

47. Rebhahn JA, Quataert SA, Sharma G, Mosmann TR. SwiftReg cluster registration automatically reduces flow cytometry data variability including batch effects. *Commun Biol* **3**, 218 (2020).

48. Blackburn MJ*, et al.* Regulatory and Helper Follicular T Cells and Antibody Avidity to Simian Immunodeficiency Virus Glycoprotein 120. *J Immunol* **195**, 3227-3236 (2015).

49. Helmold Hait S*, et al.* Early T Follicular Helper Cell Responses and Germinal Center Reactions Are Associated with Viremia Control in Immunized Rhesus Macaques. *J Virol* **93**, (2019).

50. Zhou Y*, et al.* Metascape provides a biologist-oriented resource for the analysis of systems-level datasets. *Nat Commun* **10**, 1523 (2019).

51. Qiu Z, Chu TH, Sheridan BS. TGF-beta: Many Paths to CD103(+) CD8 T Cell Residency. *Cells* **10**, (2021).

52. Lim HS, Qiu P. Quantifying Cell-Type-Specific Differences of Single-Cell Datasets Using Uniform Manifold Approximation and Projection for Dimension Reduction and Shapley Additive exPlanations. *J Comput Biol* **30**, 738-750 (2023).

53. Liao X, *et al.* Kruppel-like factor 4 regulates macrophage polarization. *J Clin Invest* **121**, 2736-2749 (2011).

54. Moso MA, *et al.* HIV latency can be established in proliferating and nonproliferating resting CD4+ T cells in vitro: implications for latency reversal. *AIDS* **33**, 199-209 (2019).

55. Neidleman J, *et al.* Phenotypic analysis of the unstimulated in vivo HIV CD4 T cell reservoir. *Elife* **9**, (2020).

56. Chitrakar A, Sanz M, Maggirwar SB, Soriano-Sarabia N. HIV Latency in Myeloid Cells: Challenges for a Cure. *Pathogens* **11**, (2022).

57. Pearce EL. Metabolism in T cell activation and differentiation. *Curr Opin Immunol* **22**, 314-320 (2010).

58. Wiercinska-Drapalo A, Flisiak R, Jaroszewicz J, Prokopowicz D. Increased plasma transforming growth factor-beta1 is associated with disease progression in HIV-1-infected patients. *Viral Immunol* **17**, 109-113 (2004).

59. Dickinson M, *et al.* Dynamics of Transforming Growth Factor (TGF)-beta Superfamily Cytokine Induction During HIV-1 Infection Are Distinct From Other Innate Cytokines. *Front Immunol* **11**, 596841 (2020).

60. Liovat AS, *et al.* Acute plasma biomarkers of T cell activation set-point levels and of disease progression in HIV-1 infection. *PLoS One* **7**, e46143 (2012).

61. Salmond RJ. Regulation of T Cell Activation and Metabolism by Transforming Growth Factor-Beta. *Biology (Basel)* **12**, (2023).

62. Regis S, Dondero A, Caliendo F, Bottino C, Castriconi R. NK Cell Function Regulation by TGF-beta-Induced Epigenetic Mechanisms. *Front Immunol* **11**, 311 (2020).

63. Zaiatz-Bittencourt V, Finlay DK, Gardiner CM. Canonical TGF-beta Signaling Pathway Represses Human NK Cell Metabolism. *J Immunol* **200**, 3934-3941 (2018).

64. Das L, Levine AD. TGF-beta inhibits IL-2 production and promotes cell cycle arrest in TCR-activated effector/memory T cells in the presence of sustained TCR signal transduction. *J Immunol* **180**, 1490-1498 (2008).

65. Chen W. TGF-beta Regulation of T Cells. *Annu Rev Immunol* **41**, 483-512 (2023).

66. Yamazaki T*, et al.* Galunisertib plus neoadjuvant chemoradiotherapy in patients with locally advanced rectal cancer: a single-arm, phase 2 trial. *Lancet Oncol* **23**, 1189-1200 (2022).

67. Harding JJ*, et al.* Phase 1b study of galunisertib and ramucirumab in patients with advanced hepatocellular carcinoma. *Cancer Med* **10**, 3059-3067 (2021).

68. Kelley RK*, et al.* A Phase 2 Study of Galunisertib (TGF-beta1 Receptor Type I Inhibitor) and Sorafenib in Patients With Advanced Hepatocellular Carcinoma. *Clin Transl Gastroenterol* **10**, e00056 (2019).

69. Melisi D*, et al.* Galunisertib plus gemcitabine vs. gemcitabine for first-line treatment of patients with unresectable pancreatic cancer. *Br J Cancer* **119**, 1208-1214 (2018).

70. Walshe TE, Saint-Geniez M, Maharaj AS, Sekiyama E, Maldonado AE, D'Amore PA. TGF-beta is required for vascular barrier function, endothelial survival and homeostasis of the adult microvasculature. *PLoS One* **4**, e5149 (2009).

71. Dvorak HF. Vascular permeability factor/vascular endothelial growth factor: a critical cytokine in tumor angiogenesis and a potential target for diagnosis and therapy. *J Clin Oncol* **20**, 4368-4380 (2002).

72. Santangelo PJ*, et al.* Early treatment of SIV+ macaques with an alpha(4)beta(7) mAb alters virus distribution and preserves CD4(+) T cells in later stages of infection. *Mucosal Immunol* **11**, 932-946 (2018).

73. Fray EJ*, et al.* Antiretroviral therapy reveals triphasic decay of intact SIV genomes and persistence of ancestral variants. *Cell Host Microbe* **31**, 356-372 e355 (2023).

74. Escobar G, Mangani D, Anderson AC. T cell factor 1: A master regulator of the T cell response in disease. *Sci Immunol* **5**, (2020).

75. Rutishauser RL*, et al.* TCF-1 regulates HIV-specific CD8+ T cell expansion capacity. *JCI Insight* **6**, (2021).

76. Choi YS*, et al.* LEF-1 and TCF-1 orchestrate T(FH) differentiation by regulating differentiation circuits upstream of the transcriptional repressor Bcl6. *Nat Immunol* **16**, 980-990 (2015).

77. Zheng SG, Wang J, Wang P, Gray JD, Horwitz DA. IL-2 is essential for TGF-beta to convert naive CD4+CD25- cells to CD25+Foxp3+ regulatory T cells and for expansion of these cells. *J Immunol* **178**, 2018-2027 (2007).

78. Frank I*, et al.* Blocking alpha4beta7 integrin delays viral rebound in SHIVSF162P3-infected macaques treated with anti-HIV broadly neutralizing antibodies. *Sci Transl Med* **13**, (2021).

79. Pertea M, Kim D, Pertea GM, Leek JT, Salzberg SL. Transcript-level expression analysis of RNA-seq experiments with HISAT, StringTie and Ballgown. *Nat Protoc* **11**, 1650-1667 (2016).

80. Love MI, Huber W, Anders S. Moderated estimation of fold change and dispersion for RNA-seq data with DESeq2. *Genome Biol* **15**, 550 (2014).

FIGURE LEGENDS

Figure 1. Four 2-weeks cycles with galunisertib lead to viral reactivation in blood. A) Schematic representation of the study and sampling schedule B) Plasma VL in blood for each macaque throughout the study. The longer black line indicates the period on ART, while the 4 small black lines indicate the start and end of each galunisertib cycle. C) Enlarged plasma VL for all macaques during galunisertib therapy. Green bars indicate galunisertib cycles. Source data are provided as a Source Data file. Image from BioRender.

Figure 2. Galunisertib leads to viral reactivation in tissues. A) The ^{64}Cu-DOTA-Fab$_2$(7D3) probe was injected ~24hrs before PET/CT scan before and at the end of each of the first 3 galunisertib cycles. Representative images from the maximum intensity projections (MIP) of fused PET and CT scans are shown for a macaque with a major increase at the end of cycle 2 and one showing increase at the beginning of cycle 3. MIPs were generated using the MIM software, set to a numerical scale of 0-1.5 SUVbw and visualized with the *Rainbow* color scale. B) Mean SUV were calculated for each anatomical area and values analyzed with mixed-effect analysis. Data from the scans performed at the last 2 time points (BC3 and AC3) in 08M171 were excluded because of technical issues with the probe. Thicker black line represents the mean. P–values were calculated for comparison of each time point with the before cycle 1 time point (BC1; AC1= after cycle 1, BC2= before cycle 2; AC2= after cycle 2; BC3= before cycle 3; AC3= after cycle 3; Holm-Sidak multiple comparison correction; *p≤0.05 **p≤0.01 ***p≤0.01). Source data are provided as a Source Data file.

Figure 3. Galunisertib decreases viral reservoir in absence of systemic inflammation. A) Levels of cell-associated (CA)-vDNA per cell equivalent are shown for the time point before cycle 1 (BC1) and at the end of cycle 3 (AC3) or 4 (AC4) for the respective tissues for all 8 macaques. B) IPDA data are shown for intact and total provirus for BC1 and AC4 in PBMC for the 8

macaques. P-values are shown for Wilcoxon matched pair signed-rank non-parametric two-tailed test comparing before and after galunisertib data from the 8 macaques (*p≤0.05 **p≤0.01 ***p≤0.01) C) Heat map of cytokine concentration in plasma at the indicated time point are shown after Log transformation and normalization. Statistical analysis was run on each factor separately and together (no significant differences after multiple comparison adjustment). Source data are provided as a Source Data file.

Figure 4. Galunisertib leads toward effector in T and NK cells, increasing Treg and decreasing Tfh frequencies. A-F) Geometric mean fluorescent intensities (MFI) of each marker and frequency of indicated subset within live, singlets $CD3^+$ $CD4^+$ T cells (A and C) or $CD3^+$ $CD4^+$ $CD95^+$ T cells (B) or $CD8^+$ or $CD8^+$ $CD95^+$ T cells or NK cells ($NKG2A^+$ $CD8^+$ $CD3^-$ cells) are shown. Thick black line represents the mean. Changes from baseline (beginning of cycle 1, BC1) are shown for graphs with at least 1 significant difference (Repeated measures ANOVA with Holm-Sidak correction for multiple comparisons; *p≤0.05 **p≤0.01 ***p≤0.01). G) tSNE of lymphocyte, live, singlets events after normalization for BC1 and AC4 (all 8 macaques) with FlowSOM 36 clusters overlaid on tSNE (top left) or heatmap of each markers MFI (right) or heatmap of time point (blue is BC1 and red is AC4; bottom left) is shown. 6 populations were manually gated on red or blue areas (red, New1-3 and blue Old1-3). H) Bubble chart displaying changes in AC4 from BC1 in populations (FlowSOM clusters) characterized by markers MFI in Fig S8A. Color is proportional to the effect size and size to p-value (Wilcoxon sum rank non-parameter two-tailed test). I) Bubble chart displaying changes from BC1 at all time points in populations (FlowSOM clusters) characterized in Fig S8C (ANOVA repeated measures with Holm-Sidak multiple comparisons correction; *p≤0.05 **p≤0.01 ***p≤0.01). J) Frequency of indicated subset within live, singlets $CD3^+$ $CD4^+$ T or $CD3^+$ $CD4^+$ $CD95^+$ $CD28^+$ T cells (CM=central memory) or within $CD3^+$ $CD8^+$ T cells. Changes from baseline (BC1) are shown (ANOVA repeated measures with Holm-

Sidak correction for multiple comparisons; $*p \leq 0.05$ $**p \leq 0.01$ $***p \leq 0.01$). Source data are provided as a Source Data file.

Figure 5. OXPHOS and other metabolic pathways increase rapidly with TGF-β blockade. A-C) Bulk RNAseq was performed with PBMC from before cycle 1 (24hrs) and 1hrs after the first dose of galunisertib (A) or after the last dose of cycle 1 (B) and with rectal biopsies collected before cycle 1 (24hrs) and after the last dose of cycle 1 (C). The number of differentially expressed genes (DEG) obtained by DESeq2 with an FDR <0.05 and abs($\log_2$FC)>2 are shown in each respective volcano plot. Enrichment plots are shown after GSEA (with all FDR<0.05 DEGs) for significantly enriched pathways (top 1 or 2 pathway by ES). C) Lollipop graph of selected DEG of interest among significantly different genes (FDR<0.05). Source data are provided as a Source Data file.

Figure 6. scRNAseq of lymph node before and after cycle 1 confirms a switch toward effector and increased metabolism in all immune subsets with galunisertib. A) UMAP projection of 93234 cells from lymph nodes collected right before and at the end of cycle 1 from all 8 macaques (16 samples). Gene-based classification of major immune subset is overlaid on UMAP. In gray are unclassified cells. B-C) Bubble plots showing expression (mean normalized counts proportional to the color; size proportional to the percentage of cells) of each marker listed in each cell subset. Marker listed are those used for classification of major immune subsets (B) or CD4$^+$ and CD8$^+$ T cells (C). D) Significantly different genes obtained by Hurdle model (FDR<0.05; log2FC=0.15) in the T cell subset are shown with color proportional to normalized counts. E) Significantly enriched pathways (FDR<0.01) in T cells DEGs within the hallmark collection. F-G) Significantly different genes (FDR<0.05; log2FC=0.15) in the CD4$^+$ (F) and CD8$^+$

(G) T cell subset. H-I) Significantly enriched pathways (FDR<0.01) in CD4$^+$ T cells DEGs within the hallmark (H) and biocarta (I) collections. Source data are provided as a Source Data file.

Figure 7. Galunisertib increases SIV-specific responses. Average spots (from triplicates) per 10^6 PBMC at the time of ART initiation (pre-ART), before cycle 1 (BC1), after cycle 1 (AC1) and at the end of cycle 3 (AC3) with galunisertib after 24hrs ex vivo stimulation with 15-mer peptides (gag, env, pol) or mock (DMSO). Each post-galunisertib time point was compared to BC1 (Mixed effect analysis adjusted for multiple comparisons with Dunnet post-hoc p-values are shown; *p≤0.05 **p≤0.01 ***p≤0.001). Bars represent the median with interquartile range as error bars. Source data are provided as a Source Data file.

Figure 8. TCF1 decrease associates with virological and immunological endpoints. A) Barcode diversity measure as Shannon Entropy is shown before and after each of the first 3 galunisertib cycles for LN, PBMC and colorectal biopsies. Box-and-whisker plot represents the median +/− the interquartile range of data from 4 to 8 macaques (all data from macaques with detectable barcodes were included at each time point for a given tissue; no significant differences using linear mixed effects models). Blue= before; Red= end of each cycle. B) Bubble plot shows the results of statistical testing (Chi-squared) for differences in frequency distribution of barcodes before compared to after, for each of the first 3 cycles of galunisertib for each macaque in the indicated tissues. Blue indicates significant differences p≤0.05. C) Barcode entropy of virus isolated at the time of ART initiation compared to week 6 post-ATI in plasma (Wilcoxon matched pairs two-tailed test; *p≤0.05). D) Correlation matrix of several key variables of virological or immunological effect of galunisertib. Color is proportional to Pearson r coefficient. *p≤0.05 **p≤0.01 ***p≤0.001 indicate significant correlations. E) Association between fold increase in TCF1 (MFI) from BC1 to AC4 with CA-vDNA levels at AC4, change in gut SUV at AC3 compared

to BC1 and fold increase in IFN-γ (AC3 vs BC1). Person r is shown. All correlations have *$p \leq 0.05$.

Source data are provided as a Source Data file.

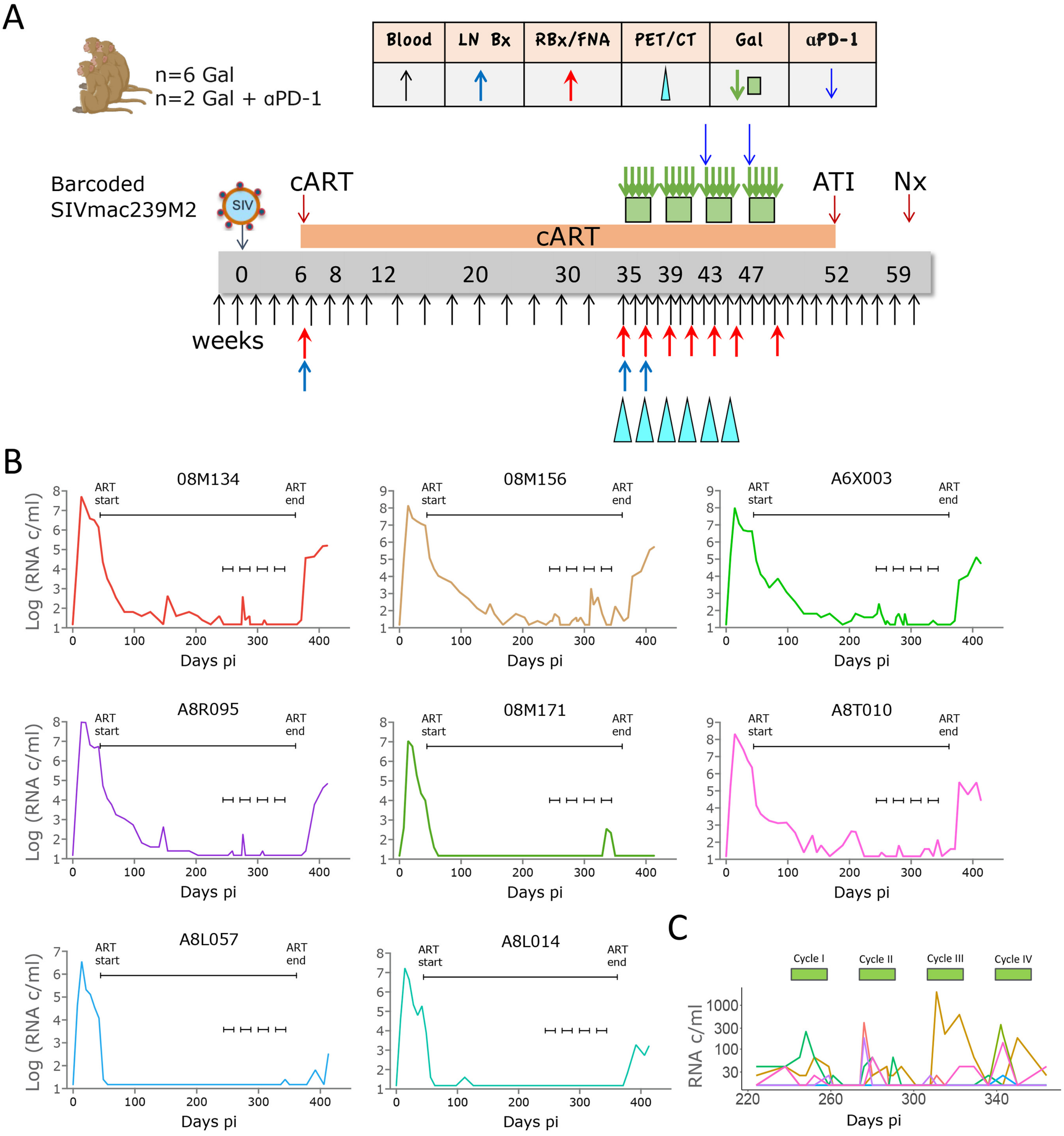
A
n=6 Gal
n=2 Gal + αPD-1
Blood
LN Bx
RBx/FNA
PET/CT
Gal
αPD-1
Barcoded SIVmac239M2
SIV
cART
ATI
Nx
cART
0
6
8
12
20
30
35
39
43
47
52
59
weeks
B
08M134
08M156
A6X003
A8R095
08M171
A8T010
A8L057
A8L014
ART start
ART end
Log (RNA c/ml)
Days pi
0
100
200
300
400
C
Cycle I
Cycle II
Cycle III
Cycle IV
RNA c/ml
1000
300
100
30
220
260
300
340
Days pi

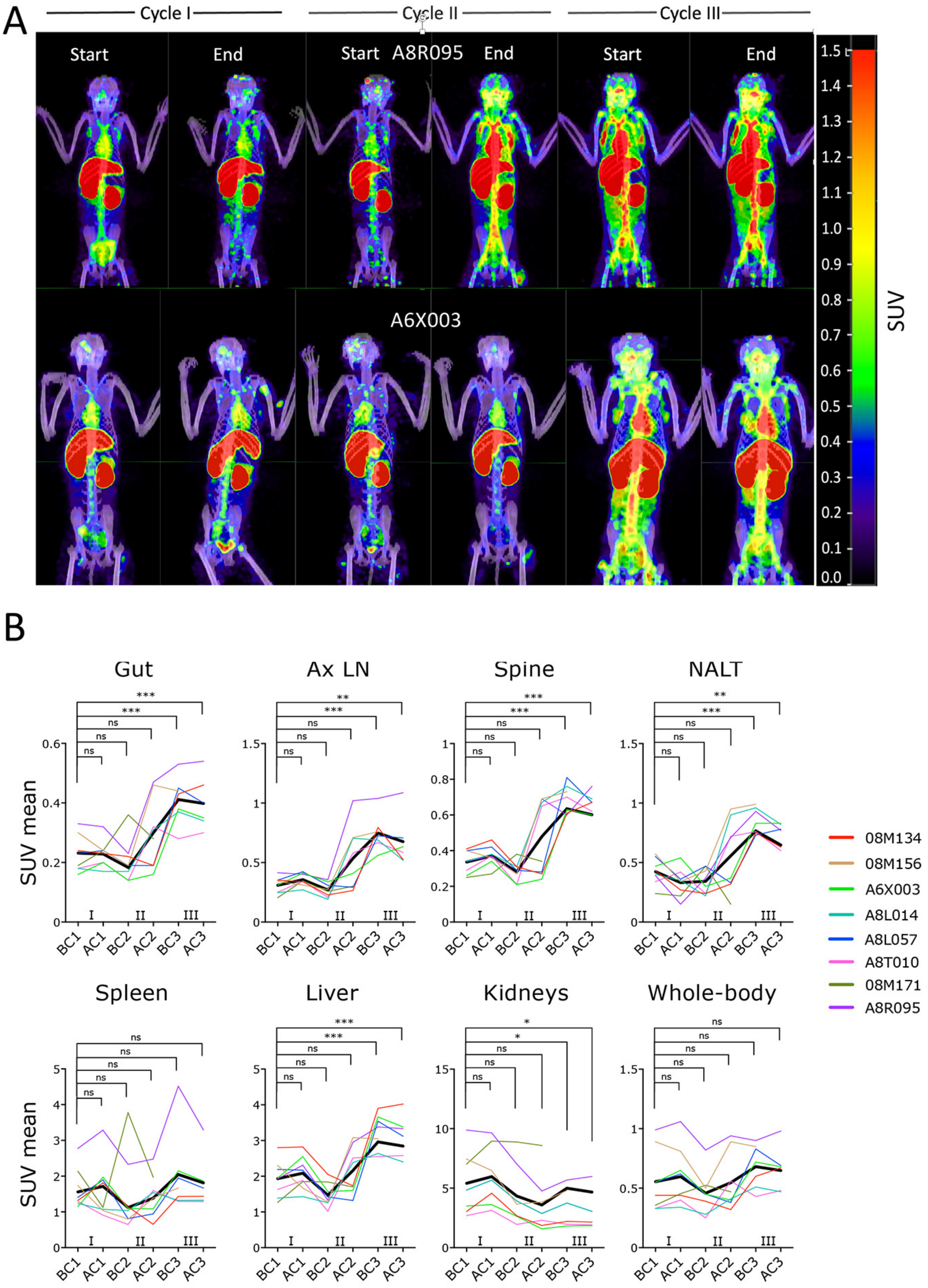
A
Cycle I
Cycle II
Cycle III
Start
End
Start
A8R095
End
Start
End
A6X003
1.5
1.4
1.3
1.2
1.1
1.0
0.9
0.8
0.7
0.6
0.5
0.4
0.3
0.2
0.1
0.0
SUV
B
Gut
Ax LN
Spine
NALT
Spleen
Liver
Kidneys
Whole-body
SUV mean
ns
**
***
*
I
II
III
BC1
AC1
BC2
AC2
BC3
AC3
08M134
08M156
A6X003
A8L014
A8L057
A8T010
08M171
A8R095

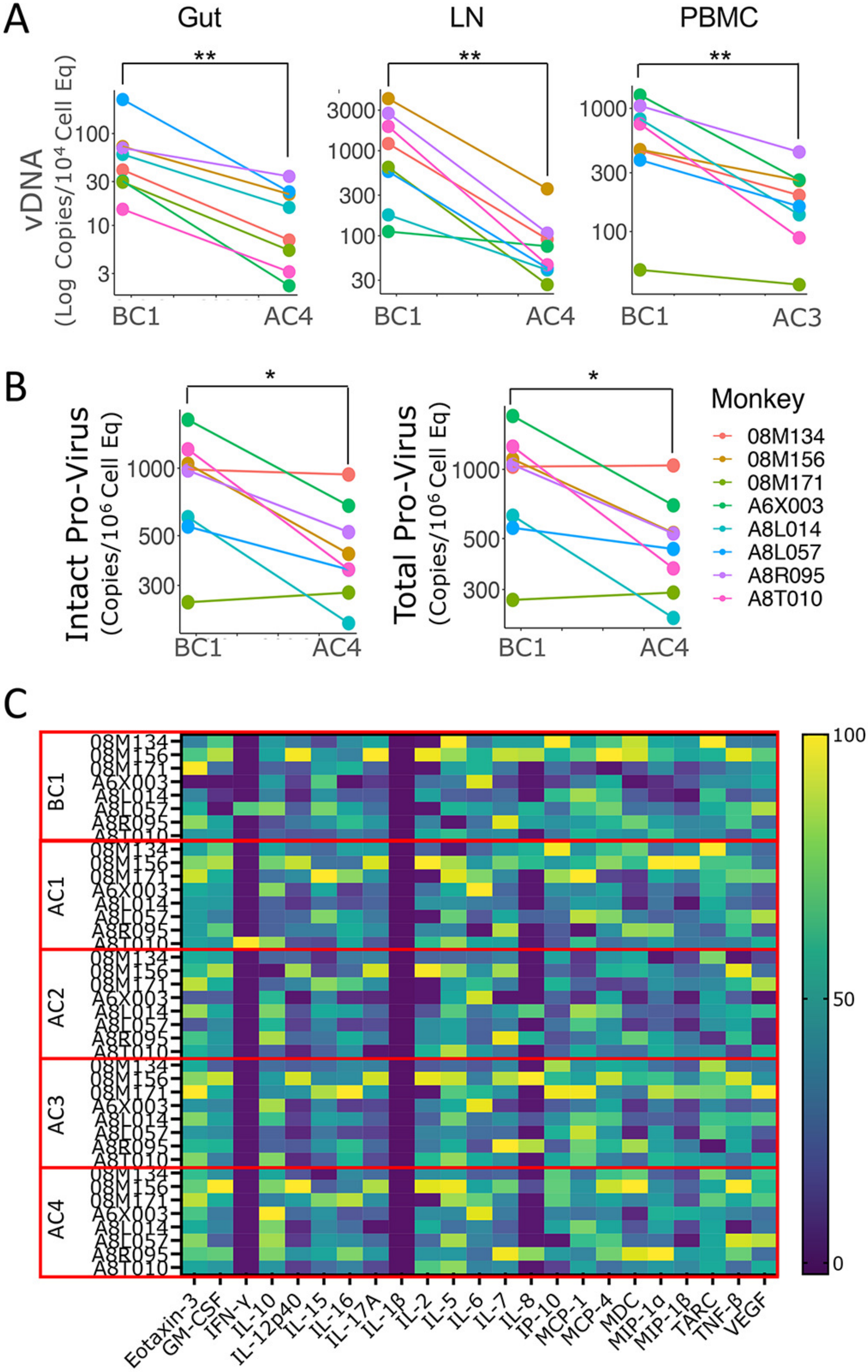
A
Gut
LN
PBMC
**
**
**
vDNA
(Log Copies/10^4 Cell Eq)
3
10
30
100
30
100
300
1000
3000
100
300
1000
BC1
AC4
BC1
AC4
BC1
AC3
B
*
*
Intact Pro-Virus
(Copies/10^6 Cell Eq)
300
500
1000
Total Pro-Virus
(Copies/10^6 Cell Eq)
300
500
1000
BC1
AC4
BC1
AC4
Monkey
08M134
08M156
08M171
A6X003
A8L014
A8L057
A8R095
A8T010
C
BC1
AC1
AC2
AC3
AC4
08M134
08M156
08M171
A6X003
A8L014
A8L057
A8R095
A8T010
Eotaxin-3
GM-CSF
IFN-γ
IL-10
IL-12p40
IL-15
IL-16
IL-17A
IL-1β
IL-2
IL-5
IL-6
IL-7
IL-8
IP-10
MCP-1
MCP-4
MDC
MIP-1α
MIP-1β
TARC
TNF-β
VEGF
100
50
0

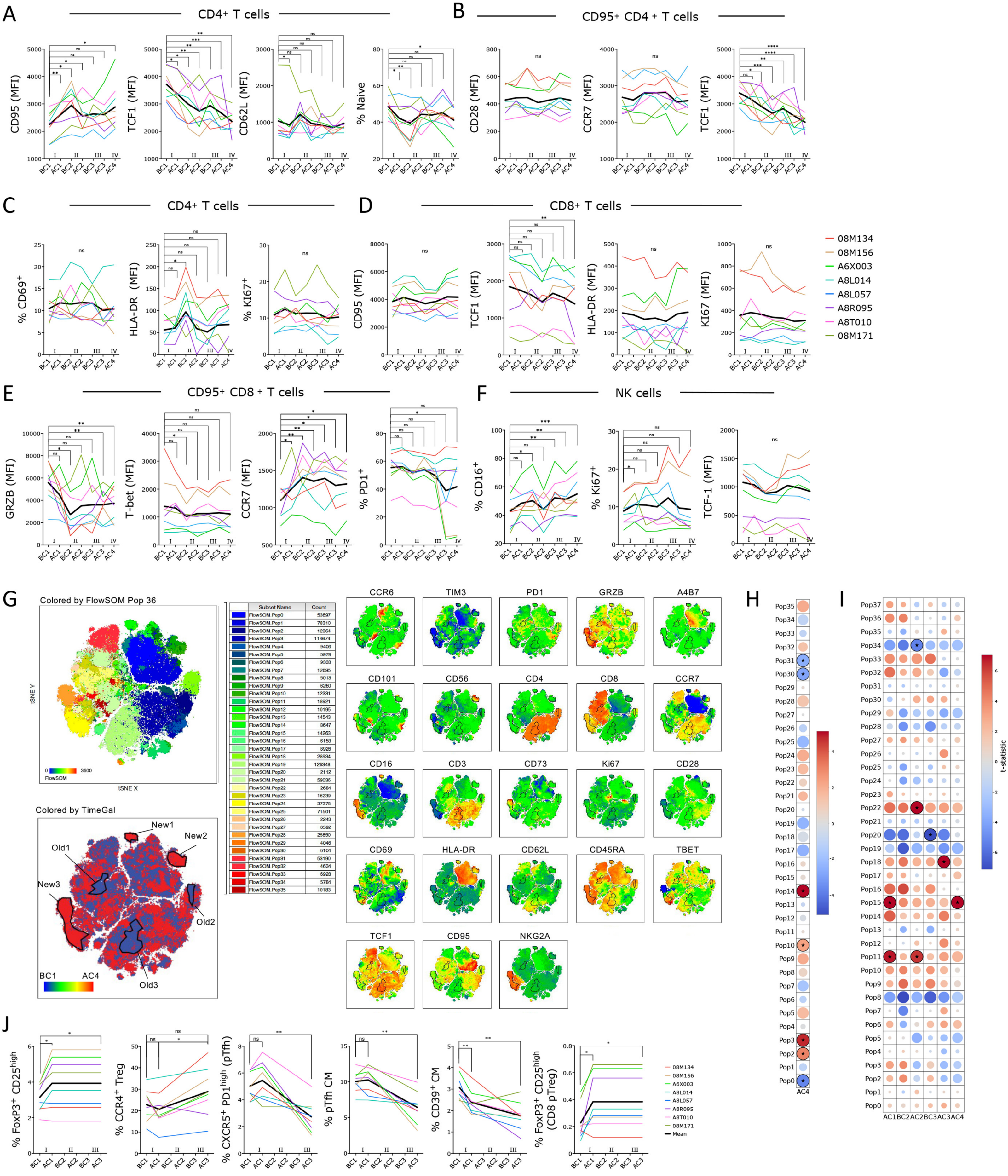

	Subset Name	Count
🟦	FlowSOM.Pop0	53697
🟦	FlowSOM.Pop1	78310
🟦	FlowSOM.Pop2	12364
🟦	FlowSOM.Pop3	114674
🟦	FlowSOM.Pop4	9406
🟦	FlowSOM.Pop5	5978
🟩	FlowSOM.Pop6	9333
🟩	FlowSOM.Pop7	12695
🟩	FlowSOM.Pop8	5013
🟩	FlowSOM.Pop9	6260
🟩	FlowSOM.Pop10	12331
🟩	FlowSOM.Pop11	18921
🟩	FlowSOM.Pop12	10195
🟩	FlowSOM.Pop13	14543
🟩	FlowSOM.Pop14	8647
🟩	FlowSOM.Pop15	14263
🟩	FlowSOM.Pop16	6158
🟩	FlowSOM.Pop17	8926
🟩	FlowSOM.Pop18	28934
🟩	FlowSOM.Pop19	126348
🟩	FlowSOM.Pop20	2112
🟩	FlowSOM.Pop21	59036
🟨	FlowSOM.Pop22	2684
🟨	FlowSOM.Pop23	16239
🟨	FlowSOM.Pop24	37378
🟨	FlowSOM.Pop25	71501
🟧	FlowSOM.Pop26	2243
🟧	FlowSOM.Pop27	6592
🟧	FlowSOM.Pop28	25850
🟧	FlowSOM.Pop29	4046
🟧	FlowSOM.Pop30	6104
🟥	FlowSOM.Pop31	53190
🟥	FlowSOM.Pop32	4634
🟥	FlowSOM.Pop33	6928
🟥	FlowSOM.Pop34	5784
🟥	FlowSOM.Pop35	10183

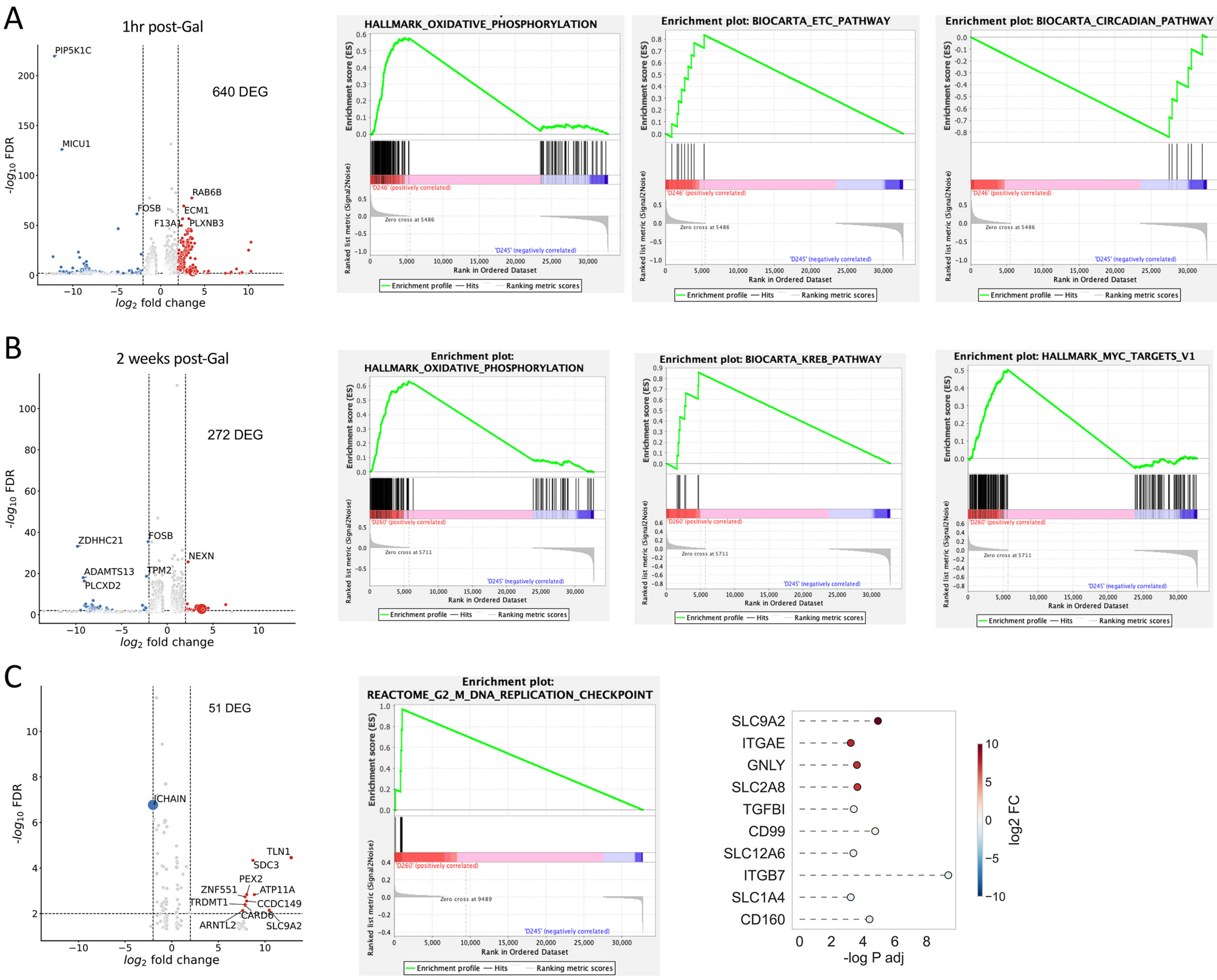
A
1hr post-Gal
640 DEG
PIP5K1C
MICU1
FOSB
F13A1
RAB6B
ECM1
PLXNB3
-log10 FDR
log2 fold change
HALLMARK_OXIDATIVE_PHOSPHORYLATION
Enrichment plot: BIOCARTA_ETC_PATHWAY
Enrichment plot: BIOCARTA_CIRCADIAN_PATHWAY
Enrichment score (ES)
Ranked list metric (Signal2Noise)
Rank in Ordered Dataset
'D246' (positively correlated)
'D245' (negatively correlated)
Zero cross at 5486
Enrichment profile
Hits
Ranking metric scores
B
2 weeks post-Gal
272 DEG
ZDHHC21
FOSB
ADAMTS13
TPM2
PLCXD2
NEXN
Enrichment plot: HALLMARK_OXIDATIVE_PHOSPHORYLATION
Enrichment plot: BIOCARTA_KREB_PATHWAY
Enrichment plot: HALLMARK_MYC_TARGETS_V1
'D260' (positively correlated)
'D245' (negatively correlated)
Zero cross at 5711
C
51 DEG
JCHAIN
TLN1
SDC3
PEX2
ZNF551
ATP11A
TRDMT1
CCDC149
CARD6
ARNTL2
SLC9A2
Enrichment plot: REACTOME_G2_M_DNA_REPLICATION_CHECKPOINT
Zero cross at 9489
SLC9A2
ITGAE
GNLY
SLC2A8
TGFBI
CD99
SLC12A6
ITGB7
SLC1A4
CD160
-log P adj
log2 FC

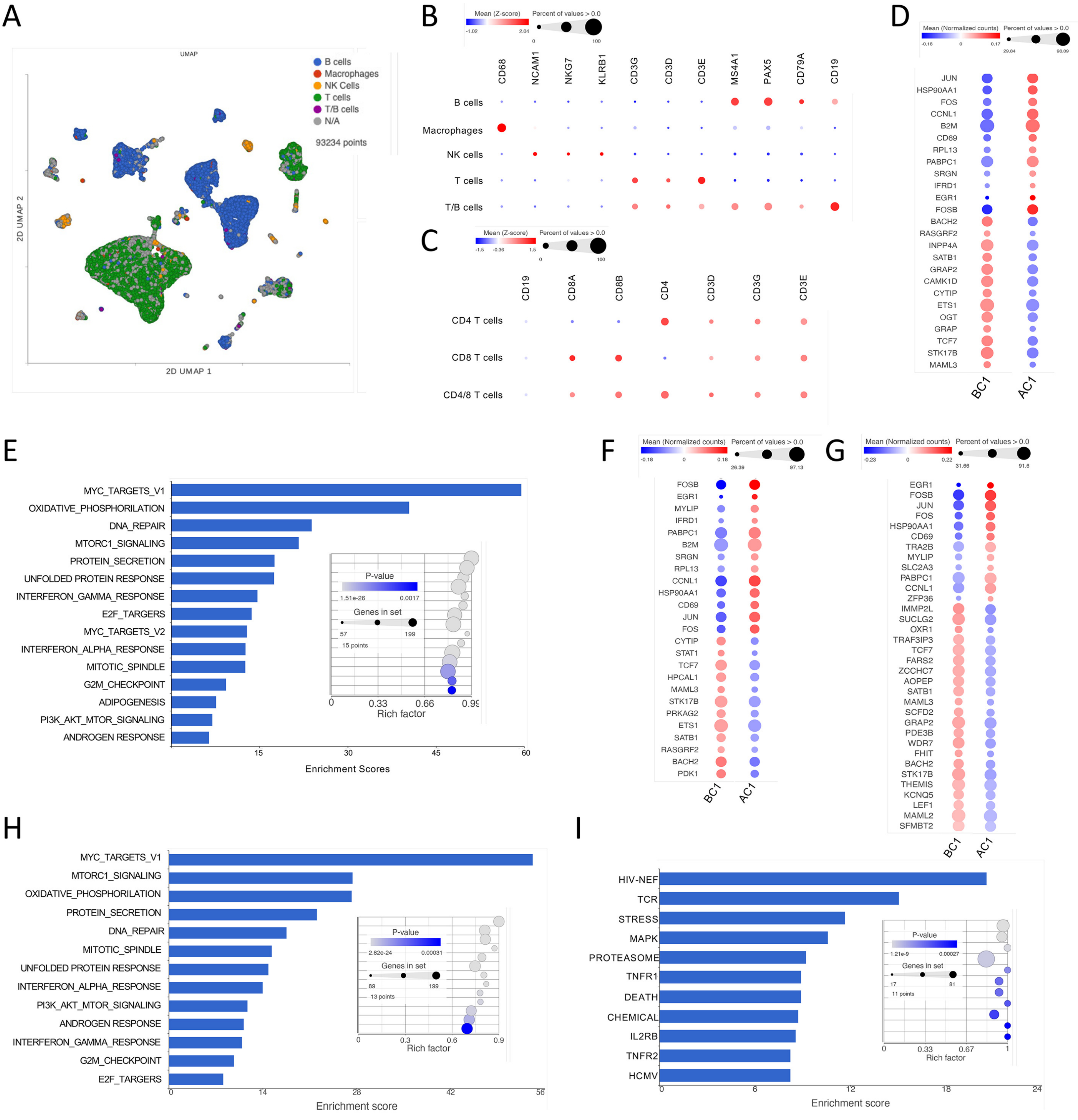
A
UMAP
B cells
Macrophages
NK Cells
T cells
T/B cells
N/A
93234 points
2D UMAP 2
2D UMAP 1
B
Mean (Z-score)
-1.02
2.04
Percent of values > 0.0
0
100
CD68
NCAM1
NKG7
KLRB1
CD3G
CD3D
CD3E
MS4A1
PAX5
CD79A
CD19
B cells
Macrophages
NK cells
T cells
T/B cells
C
Mean (Z-score)
-1.5
-0.36
1.5
Percent of values > 0.0
0
100
CD19
CD8A
CD8B
CD4
CD3D
CD3G
CD3E
CD4 T cells
CD8 T cells
CD4/8 T cells
D
Mean (Normalized counts)
-0.18
0
0.17
Percent of values > 0.0
29.84
96.09
JUN
HSP90AA1
FOS
CCNL1
B2M
CD69
RPL13
PABPC1
SRGN
IFRD1
EGR1
FOSB
BACH2
RASGRF2
INPP4A
SATB1
GRAP2
CAMK1D
CYTIP
ETS1
OGT
GRAP
TCF7
STK17B
MAML3
BC1
AC1
E
MYC_TARGETS_V1
OXIDATIVE_PHOSPHORILATION
DNA_REPAIR
MTORC1_SIGNALING
PROTEIN_SECRETION
UNFOLDED PROTEIN RESPONSE
INTERFERON_GAMMA_RESPONSE
E2F_TARGERS
MYC_TARGETS_V2
INTERFERON_ALPHA_RESPONSE
MITOTIC_SPINDLE
G2M_CHECKPOINT
ADIPOGENESIS
PI3K_AKT_MTOR_SIGNALING
ANDROGEN RESPONSE
15
30
45
60
Enrichment Scores
P-value
1.51e-26
0.0017
Genes in set
57
199
15 points
0
0.33
0.66
0.99
Rich factor
F
Mean (Normalized counts)
-0.18
0
0.18
Percent of values > 0.0
28.39
97.13
FOSB
EGR1
MYLIP
IFRD1
PABPC1
B2M
SRGN
RPL13
CCNL1
HSP90AA1
CD69
JUN
FOS
CYTIP
STAT1
TCF7
HPCAL1
MAML3
STK17B
PRKAG2
ETS1
SATB1
RASGRF2
BACH2
PDK1
BC1
AC1
G
Mean (Normalized counts)
-0.23
0
0.22
Percent of values > 0.0
31.66
91.6
EGR1
FOSB
JUN
FOS
HSP90AA1
CD69
TRA2B
MYLIP
SLC2A3
PABPC1
CCNL1
ZFP36
IMMP2L
SUCLG2
OXR1
TRAF3IP3
TCF7
FARS2
ZCCHC7
AOPEP
SATB1
MAML3
SCFD2
GRAP2
PDE3B
WDR7
FHIT
BACH2
STK17B
THEMIS
KCNQ5
LEF1
MAML2
SFMBT2
BC1
AC1
H
MYC_TARGETS_V1
MTORC1_SIGNALING
OXIDATIVE_PHOSPHORILATION
PROTEIN_SECRETION
DNA_REPAIR
MITOTIC_SPINDLE
UNFOLDED PROTEIN RESPONSE
INTERFERON_ALPHA_RESPONSE
PI3K_AKT_MTOR_SIGNALING
ANDROGEN RESPONSE
INTERFERON_GAMMA_RESPONSE
G2M_CHECKPOINT
E2F_TARGERS
0
14
28
42
56
Enrichment score
P-value
2.82e-24
0.00031
Genes in set
89
199
13 points
0
0.3
0.6
0.9
Rich factor
I
HIV-NEF
TCR
STRESS
MAPK
PROTEASOME
TNFR1
DEATH
CHEMICAL
IL2RB
TNFR2
HCMV
0
6
12
18
24
Enrichment score
P-value
1.21e-9
0.00027
Genes in set
17
81
11 points
0
0.33
0.67
1
Rich factor

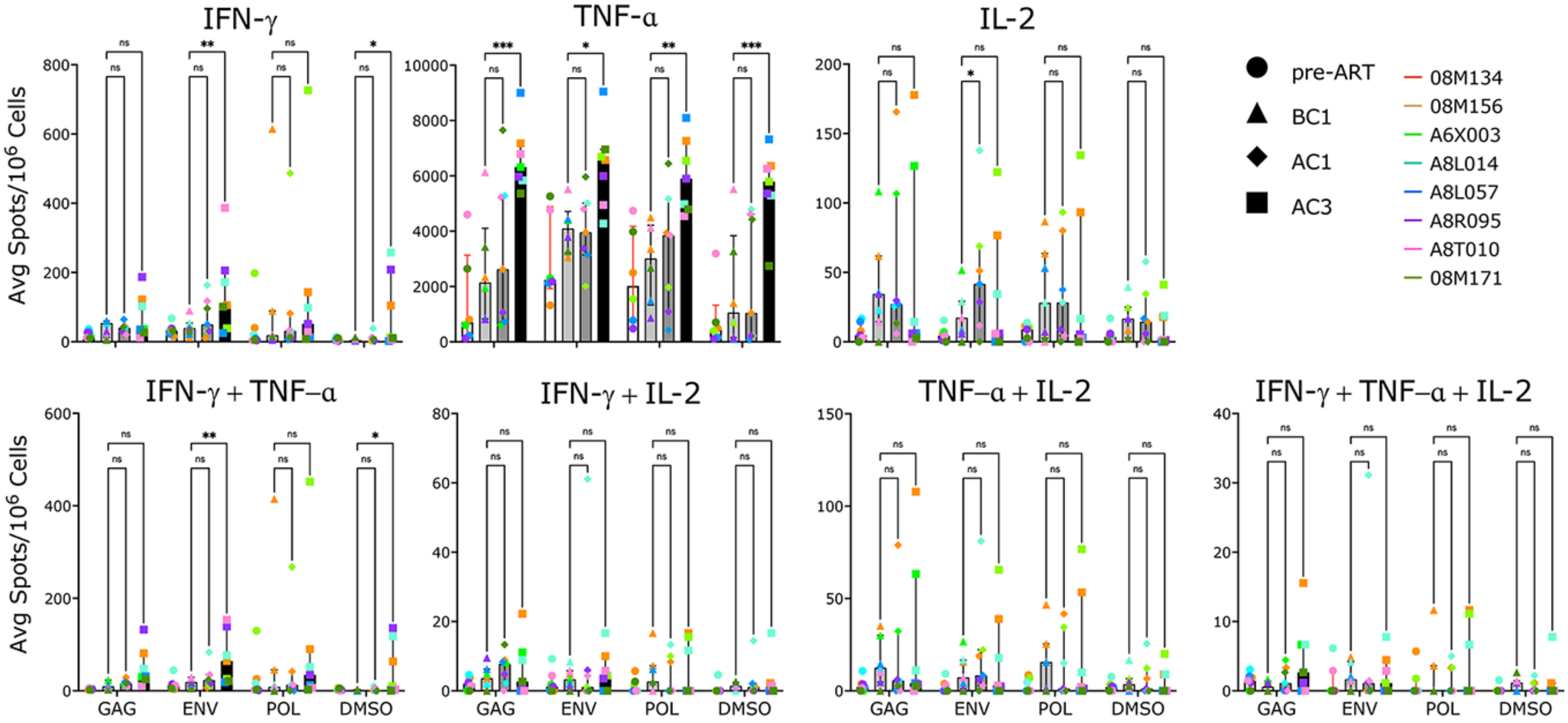
IFN-γ
TNF-α
IL-2
IFN-γ + TNF–α
IFN-γ + IL-2
TNF–α + IL-2
IFN-γ + TNF–α + IL-2
Avg Spots/10^6 Cells
GAG
ENV
POL
DMSO
ns
*
**
***
pre-ART
BC1
AC1
AC3
08M134
08M156
A6X003
A8L014
A8L057
A8R095
A8T010
08M171

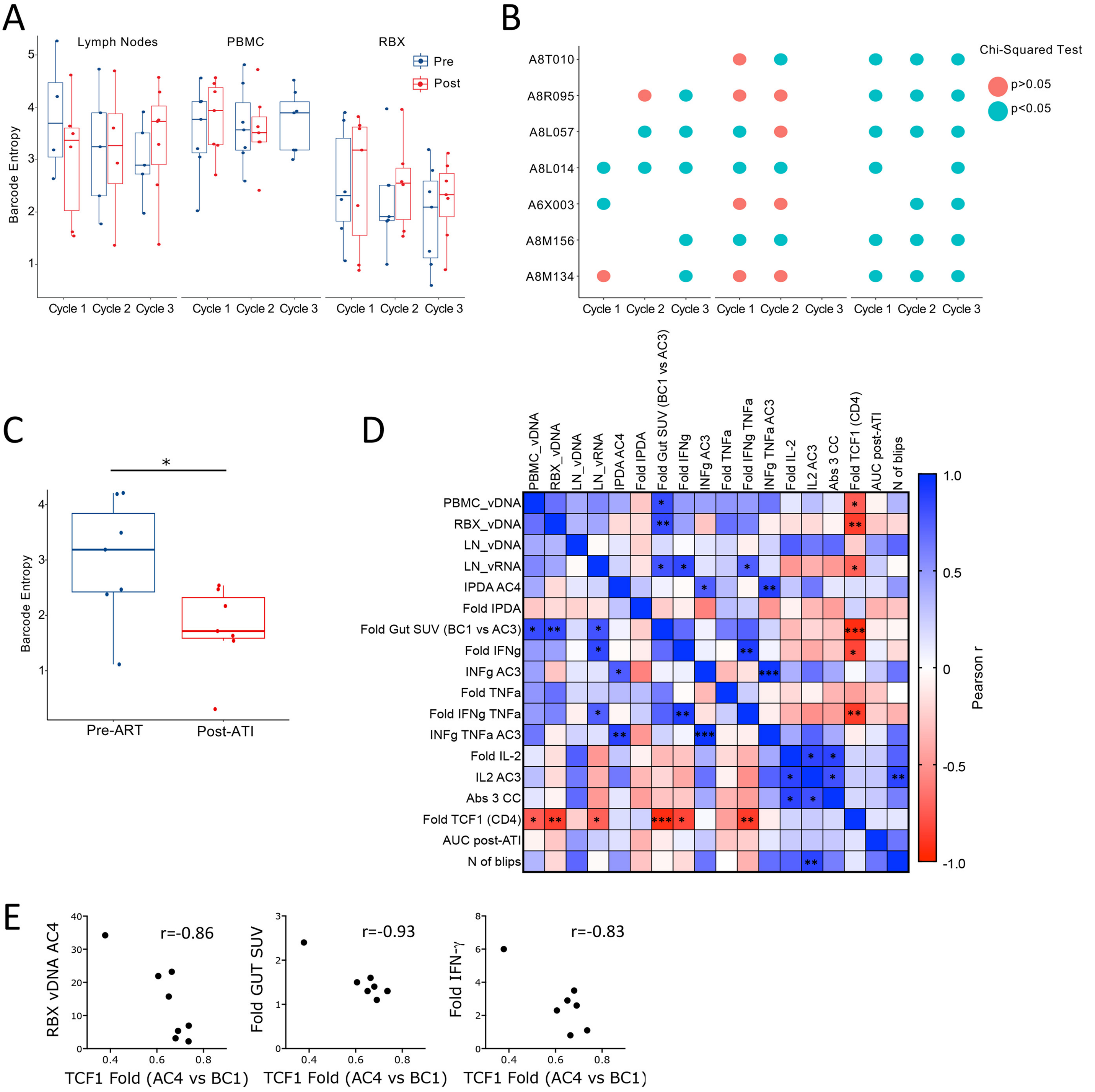
A
Lymph Nodes
PBMC
RBX
Pre
Post
Barcode Entropy
1
2
3
4
5
Cycle 1
Cycle 2
Cycle 3
B
Chi-Squared Test
p>0.05
p<0.05
A8T010
A8R095
A8L057
A8L014
A6X003
A8M156
A8M134
Cycle 1
Cycle 2
Cycle 3
C
*
Barcode Entropy
Pre-ART
Post-ATI
D
PBMC_vDNA
RBX_vDNA
LN_vDNA
LN_vRNA
IPDA AC4
Fold IPDA
Fold Gut SUV (BC1 vs AC3)
Fold IFNg
INFg AC3
Fold TNFa
Fold IFNg TNFa
INFg TNFa AC3
Fold IL-2
IL2 AC3
Abs 3 CC
Fold TCF1 (CD4)
AUC post-ATI
N of blips
Pearson r
1.0
0.5
0
-0.5
-1.0
E
RBX vDNA AC4
r=-0.86
Fold GUT SUV
r=-0.93
Fold IFN-γ
r=-0.83
TCF1 Fold (AC4 vs BC1)
0.4
0.6
0.8